


## Article

# A Thorough Investigation of the Dynamic Properties of Granite under Cyclic Loading

Xiaobin Ding <sup>1,2</sup> , Junxing Zhao <sup>1</sup>, Yaojun Dong <sup>1</sup> and Mi Zhou <sup>1,\*</sup>

<sup>1</sup> School of Civil Engineering and Transportation, South China University of Technology, Guangzhou 510641, China; dingxb@scut.edu.cn (X.D.); junxingzzz@outlook.com (J.Z.); 202121008752@mail.scut.edu.cn (Y.D.)

<sup>2</sup> Guangdong Provincial Key Laboratory of Modern Civil Engineering Technology, South China Institute of Geotechnical Engineering, Guangzhou 510640, China

\* Correspondence: zhoumi@scut.edu.cn

**Abstract:** We propose a novel inverse analysis method that utilizes shockwaves to detect the operational condition of tested rock. To achieve this back analysis, an in-depth investigation of the dynamic properties of granite specimens was conducted. The dynamic properties of the granite specimens were investigated using a triaxial cyclic loading machine, under different confining pressures, loading frequencies, stress amplitudes, and numbers of cycles, and a dynamic response model was constructed from the test data. The results show that the dynamic elastic modulus increased with the increase in confining pressure, while its damping ratio decreased. The dynamic elastic modulus and damping ratio increased with the increase in loading frequency. As the dynamic stress amplitude increased, the dynamic elastic modulus of the granite increased, but the dynamic damping ratio decreased. As the number of cycles increased, the dynamic elastic modulus and dynamic damping ratio of the granite decreased and gradually stabilized. The modified Duncan–Chang model was used to construct the dynamic response model of the specimens. It is worth saying that the correlation coefficient of the model is low at a loading frequency of 20 Hz. This indicates that the frequency has a greater effect on the dynamic response of the specimen compared with the confining pressure. The conclusions obtained from these tests can be used to study more comprehensively the interaction and causal relationship between different factors, and to prepare for the next steps of tunnel rock stress-state prediction.

**Keywords:** cyclic loading; confining pressure; loading frequency; dynamic stress amplitude; number of cycles; dynamic response model



**Citation:** Ding, X.; Zhao, J.; Dong, Y.; Zhou, M. A Thorough Investigation of the Dynamic Properties of Granite under Cyclic Loading. *Appl. Sci.* **2023**, *13*, 12514. <https://doi.org/10.3390/app132212514>

Academic Editors: Meng Li, Peng Huang and Nan Zhou

Received: 26 September 2023  
Revised: 6 November 2023  
Accepted: 11 November 2023  
Published: 20 November 2023



**Copyright:** © 2023 by the authors. Licensee MDPI, Basel, Switzerland. This article is an open access article distributed under the terms and conditions of the Creative Commons Attribution (CC BY) license (<https://creativecommons.org/licenses/by/4.0/>).

## 1. Introduction

Tunnel rock experiences a complex state of stress under natural conditions. The stress state can change the mechanical properties of the tunnel rock, leading to cracking of the tunnel rock and causing accidents. For example, rock dislodgement in the Sasago Tunnel in Japan posed a serious threat to people's personal safety in 2012 [1]. Therefore, it is important to know the working state of tunnel rocks for the detection and prediction of tunnel hazards.

Many researchers have found that changes in stress within a rock mass can cause changes in the detected wave velocities. Crampin et al. [2] concluded that the anisotropy of elastic wave velocities in rock masses at different stress levels is caused by microcracks. Bai et al. [3] developed a numerical microstructural model that found an increase in wave velocity associated with crack closure using Whitby mudstone. Tian et al. [4] measured the velocity variation of ultrasonic waves along a borehole surface before and after overcoring and performed an inverse analysis of in situ stress based on acoustoelasticity theory. This indicates that it is feasible to reflect the working state of the rock mass by obtaining the transformation of wave form traverse through rock mass.

We propose a method for detecting and predicting the accurate stress state of surrounding rocks in tunnels using shockwave detection methods based on the macro-mechanical properties of the tunnel surrounding rock. Figure 1 shows the workflow of our proposed device. The mechanical attenuation characteristics of a tested rock are obtained through a shockwave emission and reception device mounted on a robotic arm, where the mechanical vibration waves are propagated inside the tested rock and then picked up by the reception device and compared with the original wave form. The current working state of the detected rock (current stress level, dynamic elastic modulus, defect degree, etc.) can be then predicted based on the collected data. Previous studies have shown that rocks exhibit different dynamic response characteristics under different confining pressures and defect states. If the dynamic response model of a given rock at a specific frequency, confining pressure range, and defect state is known, then the stress state of the target rock in the specific condition can be predicted using this model.

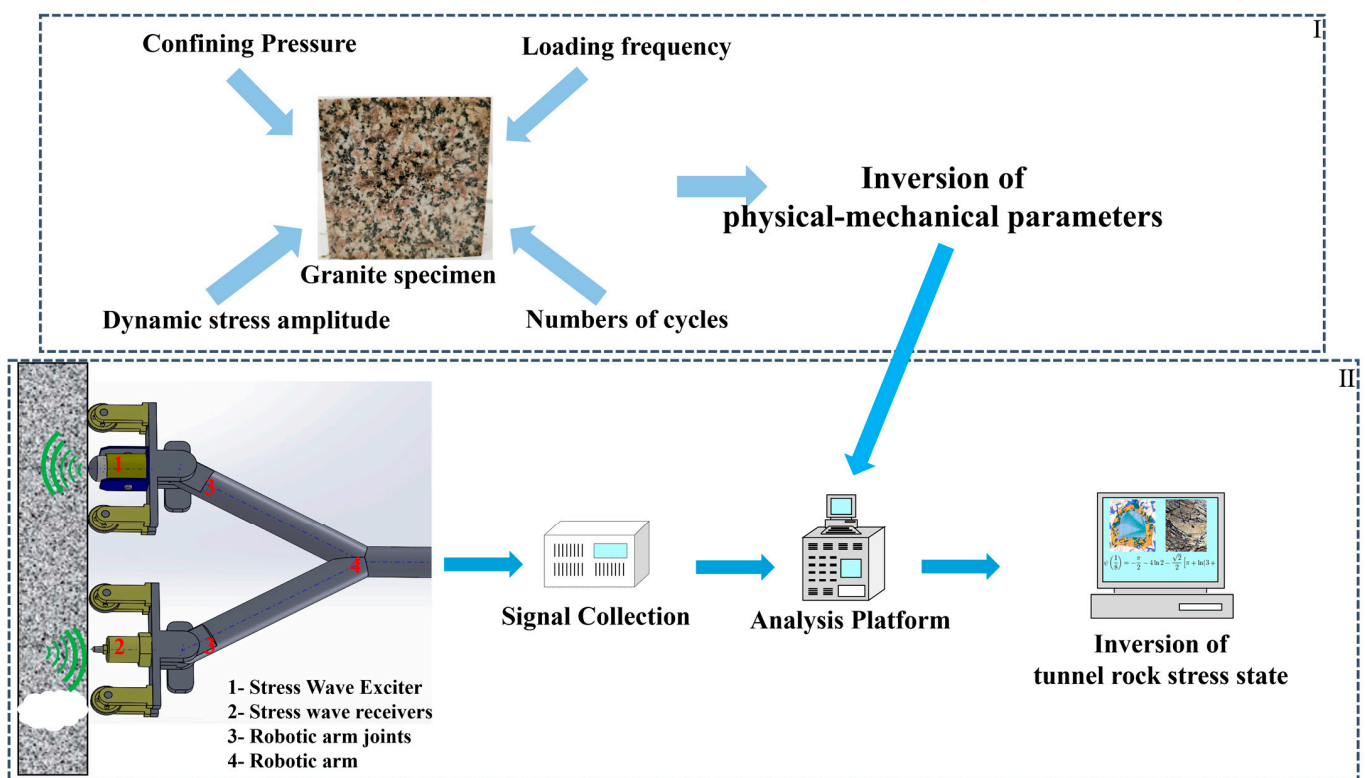
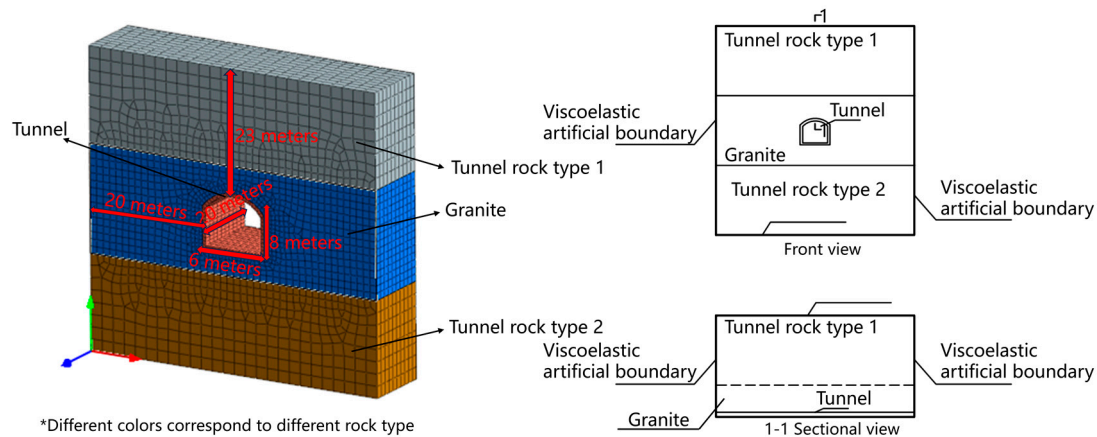


Figure 1. Illustration of the proposed workflow.

After the dynamic response behavior and an accurate constitutive model have been acquired, a simplified numerical model is built based on the test tunnel wall structure. An iterative solution process is repeated multiple times, until the stress solutions coincide for the rock wall under different loading frequency and amplitude combinations. Figure 2 shows a schematic of the target tunnel configuration. The geometry of the studied tunnel for this inspection was 6 m wide, 8 m tall, and buried 23 m deep. The boundary of the numerical model was 20 m away from the tunnel limit. The length of the tunnel excavation was 20 m, and the tunnel structure was a straight-wall arch tunnel lining structure.

We have divided the proposed study into two parts according to the sequence in which the experiments were completed. The specific research sequences are as follows: I. A literature review was conducted to determine the dynamic properties of the specimen’s influencing variables, and the dynamic properties of the rock specimen under different variables were obtained through triaxial tests. Then, a dynamic response model of the tested specimens was constructed. II. Based on the performance formula of the material obtained in part I, we were able to deduce the primary stress field of the tested tunnel

surrounding rock by combining the acquired information of the wave velocity attenuation against the known internal stress field from the triaxial test data. Thus, one of the key aims of this study was to acquire the dynamic mechanical property changes of a target rock under different controlling factors: confining pressure, loading frequency, stress amplitude, loading cycles, etc.



**Figure 2.** Schematic of target detection tunnel.

## 2. Literature Review and Discussion

Over the years, many scholars have conducted many experiments and found that many factors can affect the dynamic properties of rocks [5–13]. Gao et al. [14] analyzed intact and jointed rock specimens and found that the peak loads of jointed rock bodies with different joint inclinations decreased with decreasing strength-reduction factors. As’habi et al. [15] numerically analyzed intact and jointed rock samples under uniaxial loading and constraints using the discrete element method, focusing on the ultimate strength and fracture modes of the rocks. Ma et al. [16] found that the failure mode of coal was dependent on confining pressure. Yang et al. [17] found that the dynamic shear modulus and damping ratio of granite increased with increasing confining pressure using cyclic triaxial loading. Ma et al. [18] found that the dynamic compressive strength and elastic modulus of the coal–rock body increased with increasing confining pressure at low and high strain rates. Yan et al. [19] studied the dynamic mechanical properties of sandstone under strain and different low temperatures. Yu et al. [20] established the relationship between dynamic and static Young’s modulus and Poisson’s ratio and obtained the in situ stress profile of sandstone–shale, adjusting fracturing parameters to inform the design of multilayer interstrata fracturing. Su et al. [21] studied the influence of the joint roughness coefficient and impact strain rate on jointed rocks. Wang et al. [8] found that the fatigue life of gypsum-like rocks increased and then decreased with increasing frequency, and the energy dissipation of specimens in loading increased with increasing loading frequency. Ni et al. [22] conducted uniaxial cyclic fatigue tests on granite and found that the dynamic elastic modulus and damping ratio of granite increased with increasing cyclic frequency. Fu et al. [23] found that the elastic modulus of sandstone increased with the cyclic amplitude and cyclic frequency of the cyclic loading. Luo et al. [24] studied four types of reef limestone and obtained the correlations of physical properties of reef limestone and its dynamic and static parameters. Mishra et al. [25] found that the dimensions of phyllite and the split Hopkinson pressure bar (SHPB) loading characteristics had impact on the phyllite response. Han et al. [26] found that inclusions embedded in rock materials affected their mechanical response and fracture behavior. Liu et al. [27] obtained the effects of different frequencies, maximum stresses, and amplitudes on the fatigue mechanical properties of intermittently jointed rocks under cyclic loading. Manogharan et al. [28] obtained the nonlinear elastodynamic response of dry intact, dry fractured, and saturated fractured granite by testing at different stress amplitudes. He et al. [29] performed cyclic loading tests on sandstone and found that

with decreasing stress amplitude, moisture content had less of an effect on dynamic shear modulus and more of an effect on the damping parameters. Mishra et al. [30] used a split Hopkinson pressure bar device to study the effect of the mineralogy of granite on peak stress and the dynamic elastic modulus under varying strain rates. The results showed that the peak stress and the strain rate of the granite increased but the dynamic elastic modulus remained almost constant. Guo et al. [31] used a split Hopkinson pressure bar device to study the temperature-dependent changes in peak stress, peak strain, and elastic modulus of granite. It was found that the values of peak stress and elastic modulus decreased with increasing pre-heating temperature, while the values of peak strain increased with increasing pre-heating temperature. Wang et al. [32] investigated the dynamic properties of granite under static–cyclic impact loading and found that the confining pressure had no significant effect on the dynamic elastic modulus and that the damage mode was mainly tensile damage. Wang et al. [33] investigated the effects of stress level, strain amplitude, and loading frequency on the damping ratio and damping coefficient of granite and sandstone. It was found that the effects of stress level and strain amplitude on damping ratio were more obvious than those of frequency, and the effect of frequency on damping coefficient was greater than that of strain amplitude and stress level.

Table 1 summarizes the experimental designs by different researchers for acquiring the dynamic properties of rock. By reviewing the literature, we found that the experiments designed by research scholars were sufficiently complete. However, there are improvements that we can make to assess the current working state of rock based on test results. For instance, most of the scholars controlled only one, two, or three experimental variables for their rock tests, which may be insufficient for our current study. Additionally, the range of variables controlled by the scholars was rather limited. We introduced more control parameters and expanded the range of parameters in the experiment. With this improved approach, we can capture trends in the dynamic properties of specimens across multiple variables and a broader range of variables. In other words, we can obtain more comprehensive data, which is essential for us to conduct inverse analysis of the data. Simultaneously, we observed from Table 1 that most experiments conducted by researchers on granite had limited controlled parameters or a narrow range of control. Obtaining trends in the dynamic properties of granite specimens under multiple variables and a wider range of variables enables a more comprehensive study of interactions and causality among different factors. It also allows us to explore a broader range of factors influencing the dynamic properties of granite. Therefore, by utilizing our existing laboratory equipment, we defined the experimental variables as follows: loading frequency (1–20 Hz), confining pressure (5–30 MPa), dynamic stress amplitude (5–27.5 MPa), number of cycles (50 times and more), and the degree of specimen defects.

**Table 1.** Summary of rock properties study.

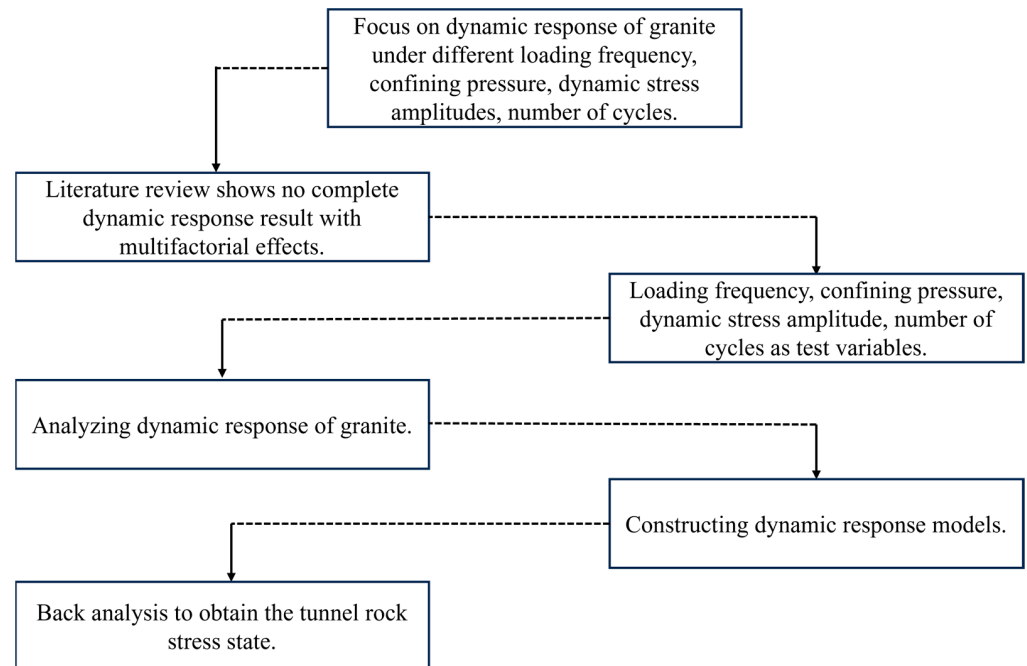
References	Rock Type	Loading Method	Variables	Parameters
Ma et al. [16]	Coal	Split Hopkinson pressure bar (SHPB) loading	Confining pressures (0–20 MPa)	Failure mode
Yang et al. [17]	Granite and red sandstone	Cyclic triaxial compression test	Confining pressures (5–25 MPa)	Dynamic shear modulus and damping ratio
Ma et al. [18]	Coal–rock	Dynamic impact test	Striking velocity (~6 m/s), confining pressures (0–15 MPa)	Dynamic compressive strength, elastic modulus
Yan et al. [19]	Sandstone	Split Hopkinson pressure bar (SHPB) loading	Temperature (−20–−1 °C)	Strength change laws and failure patterns
Su et al. [21]	Rock-like materials	Split Hopkinson pressure bar (SHPB) loading	Impact pressure (0.3–0.7 MPa), joint roughness coefficient (0–8.38)	Dynamic elastic modulus, mean dynamic compressive strength, average peak strain

Table 1. Cont.

References	Rock Type	Loading Method	Variables	Parameters
Ni et al. [22]	Granite	Cyclic loading test	Stress amplitude (10 MPa), frequency (0.01–1 Hz)	Dynamic elastic modulus, damping ratio
Fu et al. [23]	Sandstone	Cyclic loading test	Frequency (0.2–0.8 Hz), cyclic amplitudes, number of cycles	Elastic modulus
Mishra et al. [25]	Phyllite rock	Split Hopkinson pressure bar (SHPB) loading	Slenderness ratios, diameters, gas gun pressures, different striker bar lengths	Peak stress, dynamic modulus
Liu et al. [27]	Synthetic rock-like materials	Cyclic loading test	Frequency (1–20 Hz), maximum stress levels (0.8–0.95), amplitude levels (0.4–0.7)	Fatigue deformation characteristics, fatigue energy, and damage evolution
He et al. [29]	Sandstone	Cyclic loading test	Confining pressures (0.5–1 MPa), stress amplitude (0.1–0.9 MPa), moisture content (15.15–19.85%)	Damping parameters, dynamic shear modulus
Mishra et al. [30]	Granite	Split Hopkinson pressure bar (SHPB) loading	Strain rates (41.31–475.59/s)	Dynamic elastic modulus
Guo et al. [31]	Granite	Split Hopkinson pressure bar (SHPB) loading	Pre-heating temperature (25–800 °C)	Peak stress, peak strain and elastic modulus
Wang et al. [32]	Granite	Cyclic loading test	Confining pressures (2–6 MPa)	Dynamic elastic modulus
Wang et al. [33]	Granite and sandstone	Cyclic loading test	Stress level (5–25 MPa), strain amplitude (0–0.07%), frequency (0.2–0.8 Hz)	Damping ratio, damping coefficient
Li et al. [34]	Granite	Split Hopkinson pressure bar (SHPB) loading	Impact pressures (0.7–0.9 MPa), joint angle (0–90°)	Dynamic compressive strength, elastic modulus, transmitted energy ratio, absorbed energy ratio, reflected energy ratio
Chen et al. [35]	Granite residual soil	Dynamic triaxial tests	Fines content (0–83.19%), drying and wetting cycles number (1–10,000)	Dynamic shear modulus, damping ratio
Xia et al. [36]	Granite	Split Hopkinson pressure bar (SHPB) loading	Temperature (100–800 °C), axial static pressure (10–40 MPa)	Mechanical strength, elastic modulus, peak stress
Sun et al. [37]	Granite	Split Hopkinson pressure bar (SHPB) loading	Stress amplitude (48–108 MPa), cyclic upper limit stress (0.5–0.9)	Dynamic compressive strength, peak strain, transmitted energy, reflection energy
Zhang et al. [38]	Granite	Split Hopkinson pressure bar (SHPB) loading	Temperature (200–600 °C), the number of cycles (1–20 times)	Dynamic compressive strength, elastic modulus
Yan et al. [39]	Granite	Split Hopkinson pressure bar (SHPB) loading	Temperature (25–800 °C)	Dynamic peak stress, elastic modulus, peak strain
Li et al. [40]	Granite	Split Hopkinson pressure bar (SHPB) loading	Uniaxial compressive strength (0–60%), inclination angles (0–90°)	Dynamic strength
Tian et al. [41]	Granite	Split Hopkinson pressure bar (SHPB) loading	Axial pressures (0–120 MPa)	Peak stress, elastic modulus, strain rate, peak strain
Xiao et al. [42]	Granite	Split Hopkinson pressure bar (SHPB) loading	Flaw angles (0–90°), static loads (18.4–128.7 MPa)	Peak strain, dynamic strength
Li et al. [43]	Granite	Split Hopkinson pressure bar (SHPB) loading	Axial stress (0–70 MPa)	Dynamic strength, dynamic elastic modulus, dynamic strain
Chen et al. [44]	Granite	Compression tests	Confining pressure (0–5 MPa)	Elastic strains, Young's modulus
Liang et al. [45]	Granite	Split Hopkinson pressure bar (SHPB) loading	Strain rates (19.1–190.5/s)	Ultimate strength, elastic modulus
Zhao et al. [46]	Granite	Split Hopkinson pressure bar (SHPB) loading	Confining pressure (0.25–0.4 MPa)	Anti-impact strength
Current research	Granite	Dynamic triaxial tests	Confining pressure (5–30 MPa), loading frequency (1–20 Hz), dynamic stress amplitude (5–27.5 MPa), number of cycles (50 times and more)	Dynamic elastic modulus, dynamic damping ratio

This study conducted a series of cyclic loading tests on granite specimens to understand the effects of loading frequency, confining pressure, dynamic stress amplitude, and number of cycles on the dynamic properties of granite specimens, and the dynamic response model of the granite specimens was constructed. According to the degree of test completion, this paper introduces the effects of loading frequency, confining pressure, dynamic stress amplitude, and number of cycles on the dynamic characteristics of intact granite specimens and constructs the dynamic response model of granite specimens.

These data will be used for the back prediction of rock working state in the field. The test procedure is shown in Figure 3.



**Figure 3.** Workflow of this paper.

### 3. Experimental Setup

#### 3.1. Specimen Preparation

In this investigation, the granite specimens were sourced from Wulian County, Rizhao City, Shandong Province, China (Figure 4). Subsequently, the samples were precisely sectioned into cubic blocks measuring approximately 102 mm × 102 mm × 102 mm and further refined to achieve the dimensions of 100 mm × 100 mm × 100 mm.



**Figure 4.** Source of raw material for specimens.

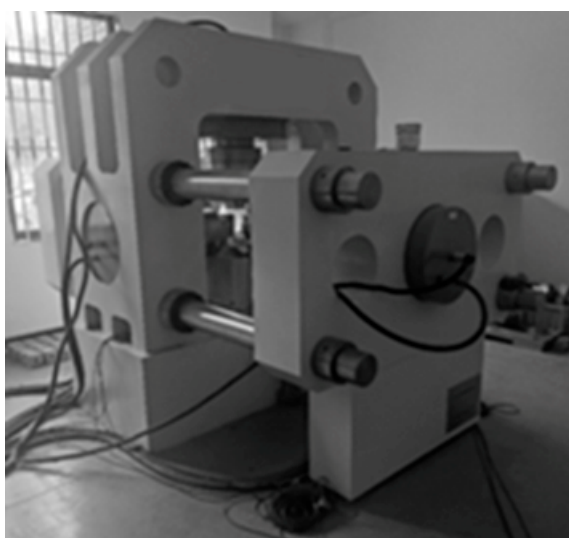
Seven specimens were prepared for this experimental investigation (Table 2). The confining pressure levels of 0, 10, 20, and 30 MPa were preselected, considering the background of tunnel engineering. Loading frequencies ranging from 1 Hz to 20 Hz were set, in accordance with the capabilities of our detection device. A similar experimental setup to that previously reported by Wang et al. [8] was adopted. The dynamic stress amplitude was predetermined within the range of 5 MPa to 27.5 MPa, accounting for the maximum pressure limit provided by the testing apparatus, while also ensuring that the specimens remained undamaged during the experimentation. The number of cycles for each test was preset at 50 cycles, reflecting the maximum number of cycles achieved before specimen failure. Each specimen is uniquely identified by a sample name, such as “Y5-10”, which indicates a specimen tested at a loading frequency of 5 Hz and a confining pressure of 10 MPa.

Table 2. Granite specimens.

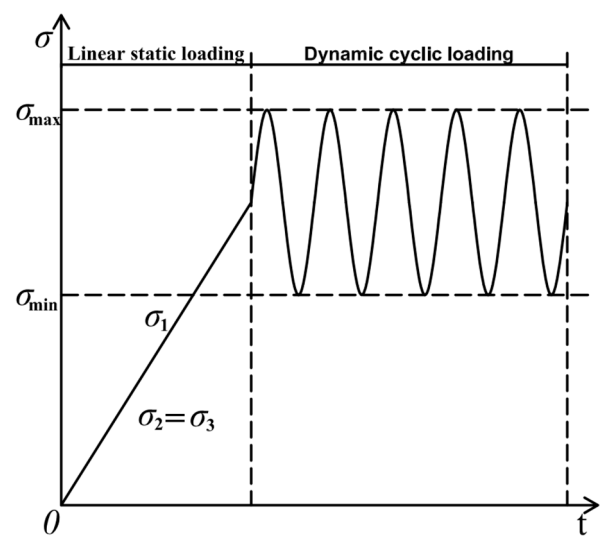
Name	Confining Pressure $\sigma_c$ (MPa)	Frequency $f$ (Hz)	Stress Amplitude $\Delta\sigma_d$ (MPa)	Number of Cycles
Y5-5	5	5	5/10/15/20/25/27.5	50
Y5-10	10			
Y5-20	20			
Y5-30	30			
Y1-20	20	1		
Y10-20		10		
Y20-20		20		

### 3.2. Test Scheme

Figure 5a displays the triaxial testing machine utilized for the experimental investigation. The machine has a maximum force capacity of 4000 kN in the vertical direction and 2400 kN in the horizontal direction. Positioned beneath the machine is the vertical dynamic loading device, designed with a maximum power capacity of 400 kN. The loading system in both the vertical and horizontal directions has a force resolution of 0.002 kN and a displacement resolution of 0.005 mm. The maximum loading speed in the horizontal direction was set at 400 mm/min.



(a)



(b)

Figure 5. Triaxial testing machine and cyclic loading scheme: (a) triaxial testing machine; (b) schematic diagram of cyclic loading.

Figure 5b illustrates the schematic representation of the uniaxial cyclic loading and unloading tests. The loading process was conducted in two stages. The initial stage involved linear static loading, characterized by a constant load rate while maintaining a pre-set confining pressure. Subsequently, the dynamic cyclic loading stage commenced, where cyclic sine wave loading was applied until the specimen experienced failure. During the loading process, variations were made to the loading frequency, dynamic stress amplitude, and number of cycles to acquire comprehensive test data.

Throughout the test loading phase, the vertical displacement acquisition device is capable of capturing a maximum of 2500 data points per second. The recorded data encompass dynamic load and dynamic displacement, which are instrumental in determining the dynamic stress and dynamic strain. Subsequently, these dynamic stress and dynamic strain values were employed in the subsequent step to ascertain the dynamic elastic modulus and dynamic damping ratio of the specimen.

### 3.3. Test Principle

Figure 6 illustrates the hysteresis loop curves for the loading and unloading processes of the specimens. The hysteresis loop characterizes the energy dissipation transpiring during the loading and unloading phases of the sample, and it can be quantified in terms of the dynamic damping ratio. The dynamic elastic modulus is defined as the tangent modulus, representing the slope of the straight or approximately linear segment of the stress–strain curve, thereby reflecting the elastic modulus of the specimen under dynamic loading conditions. The association between the dynamic elastic modulus and dynamic damping ratio is described by the following relationship [47]:

$$E_d = \frac{\sigma_{\max} - \sigma_{\min}}{\epsilon_{\max} - \epsilon_{\min}} \tag{1}$$

$$\eta = \frac{1}{4\pi} \frac{S_{ADCBA}}{S_{\Delta OEA}} = \frac{A_R}{4\pi A_S} \tag{2}$$

where  $\sigma_{\max}$  is the maximum dynamic stress,  $\sigma_{\min}$  is the minimum dynamic stress,  $\epsilon_{\max}$  is the maximum dynamic strain,  $\epsilon_{\min}$  is the minimum dynamic strain,  $A_R$  is the area of the hysteresis loop  $ADCBA$ , and  $A_S$  is the area of the triangle  $OEA$ .

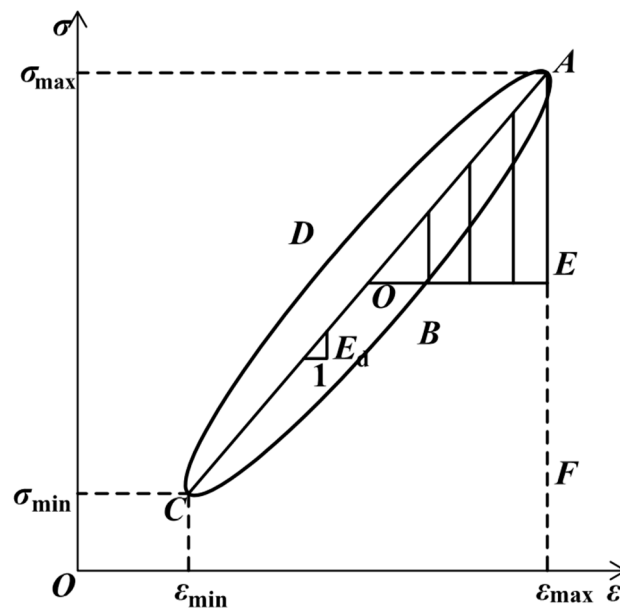


Figure 6. Dynamic stress–strain hysteresis loop.



The selected formulas have been deemed suitable and accurate for our calculations. Subsequently, we proceed to analyze the outcomes derived from these computations.

## 4. Results and Discussion

### 4.1. Hysteresis Loops of Specimens

#### 4.1.1. Effect of Confining Pressure

Figure 7 shows the relationship between dynamic stress and dynamic strain obtained from the test under different confining pressure. The dynamic stress and dynamic strain show a hysteresis loop shape under different confining pressure and dynamic stress. According to B.BJ et al. [48], the hysteresis loops of rocks under cyclic loading are generally elliptical, crescent-shaped, pointed leaf-shaped, or long eggplant-shaped. According to Figure 7, the hysteresis loop shape obtained in this test is long eggplant-shaped.

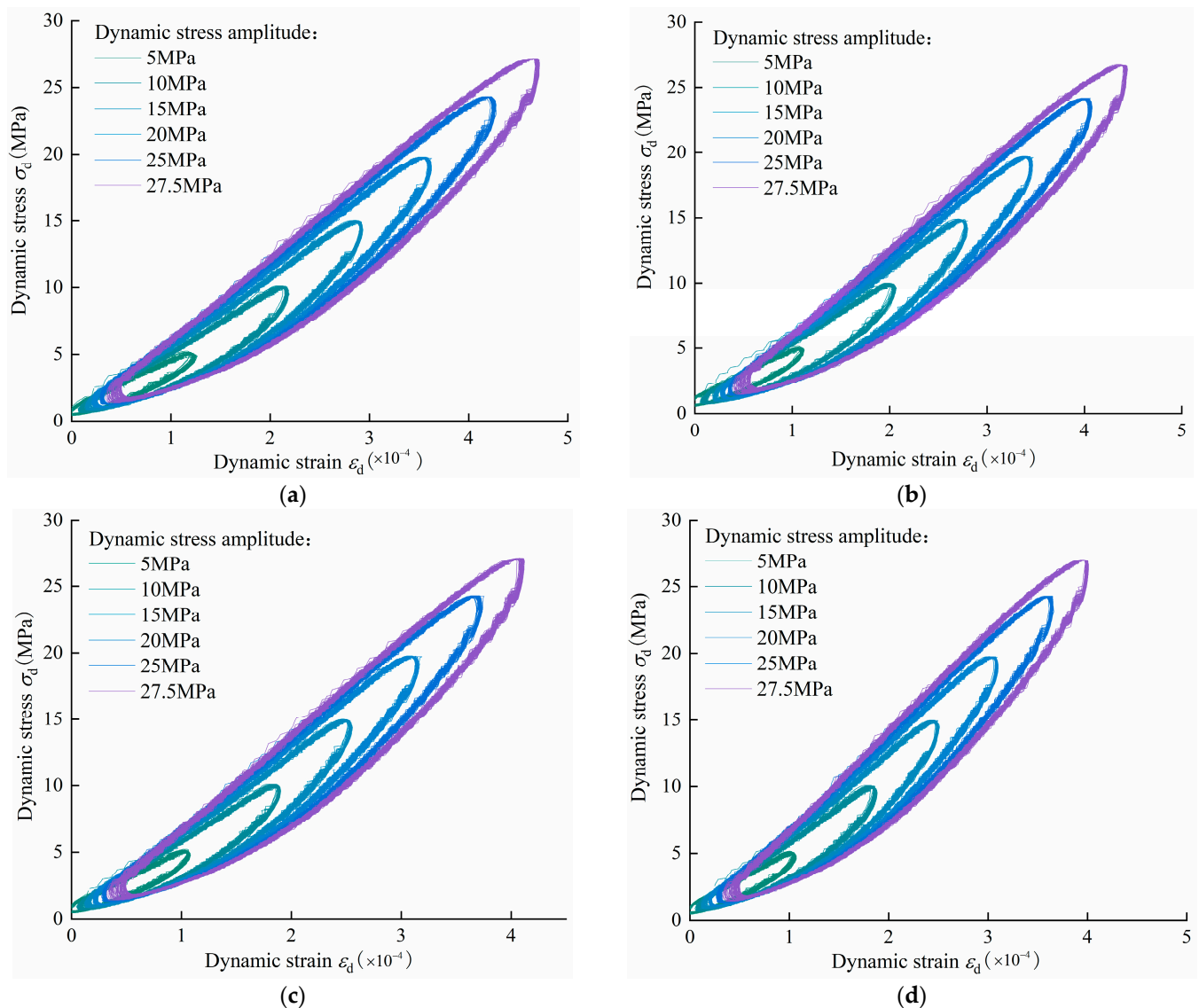


**Figure 7.** Hysteresis loop diagram: (a) Y5-5; (b) Y5-10; (c) Y5-20; (d) Y5-30.

As depicted in Figure 7, the hysteresis loop area of the specimen exhibits a reduction as the confining pressure increases under the same dynamic stress amplitude. This observation suggests a decrease in the energy dissipation of the specimen with the elevated confining pressure.

#### 4.1.2. Effect of Loading Frequency

Figure 8 illustrates the dynamic stress–strain relationship obtained from the tests conducted at different loading frequencies. The hysteresis loop curves of the specimens at high frequencies are less stable, so the hysteresis loops of the specimens at frequencies of 10 and 20 Hz show only stable curves. Additionally, with an increase in loading frequency, the hysteresis loop shape undergoes a transition from pointed leaf-shaped to elliptical, leading to expanded hysteresis loops. This observation indicates that the loading frequency influences the energy dissipation of the specimen, consequently affecting the dynamic damping ratio, which also increases with rising loading frequency. Moreover, it is noteworthy that the impact of loading frequency on the hysteresis loop of the specimen surpasses the influence of confining pressure.

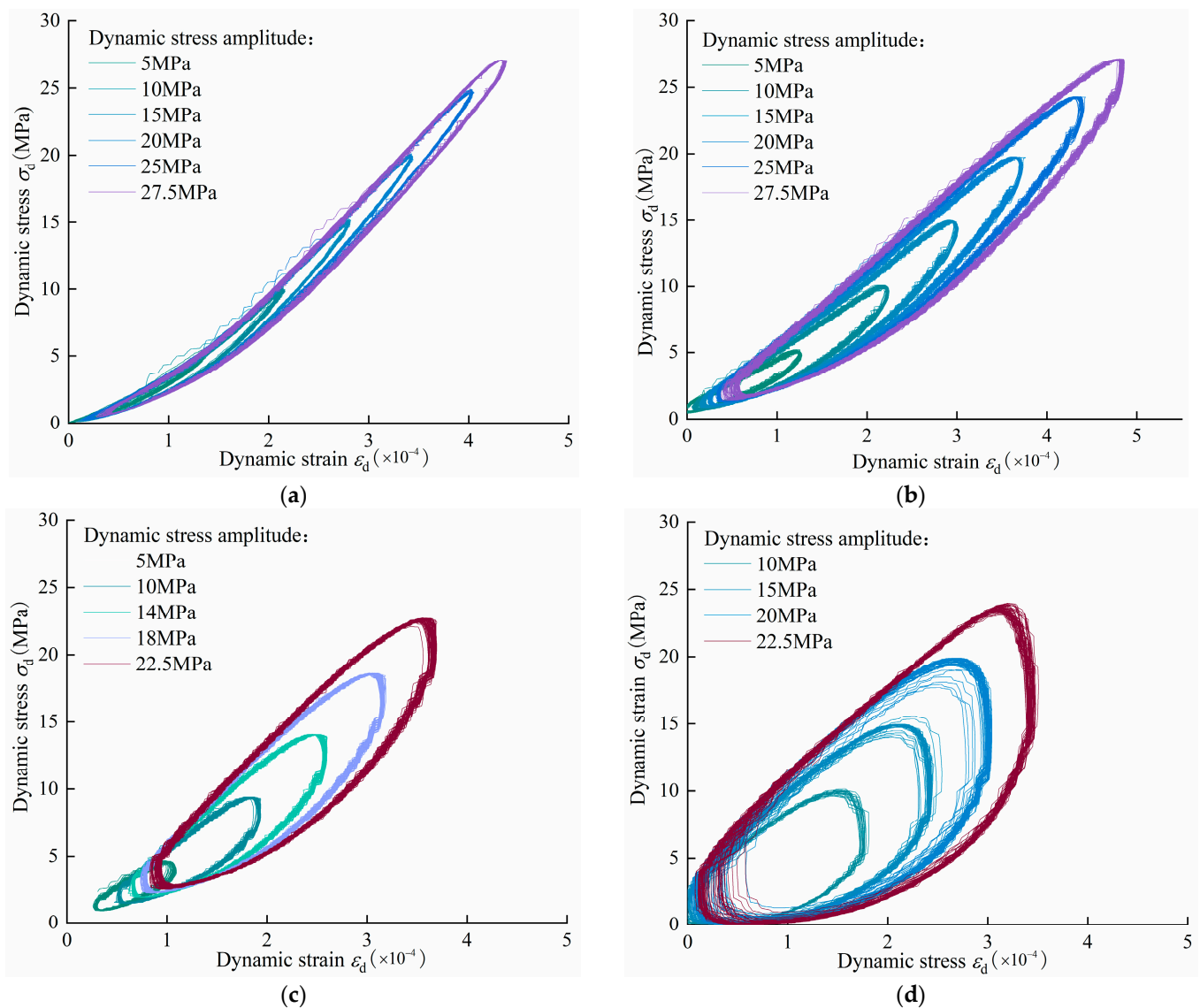


**Figure 8.** Hysteresis loop diagram: (a) Y1-20; (b) Y5-20; (c) Y10-20; (d) Y20-20.

#### 4.2. Dynamic Elastic Modulus and Dynamic Damping Ratio of Specimens

##### 4.2.1. Effect of Confining Pressure

Figure 9 presents the variations in the dynamic elastic modulus of the specimens. Figure 9a illustrates the influence of different confining pressures, dynamic stress amplitudes, and number of cycles on the dynamic elastic modulus of the specimens. It is evident that the dynamic elastic modulus of the specimens decreases with an increasing number of

cycles, while it increases with increasing confining pressure and dynamic stress amplitude. Under the same stress amplitude, the dynamic elastic modulus of the specimens exhibits a maximum increase of approximately 6% from 5 MPa to 10 MPa, about 13% from 5 MPa to 20 MPa, and approximately 20% from 5 MPa to 30 MPa.

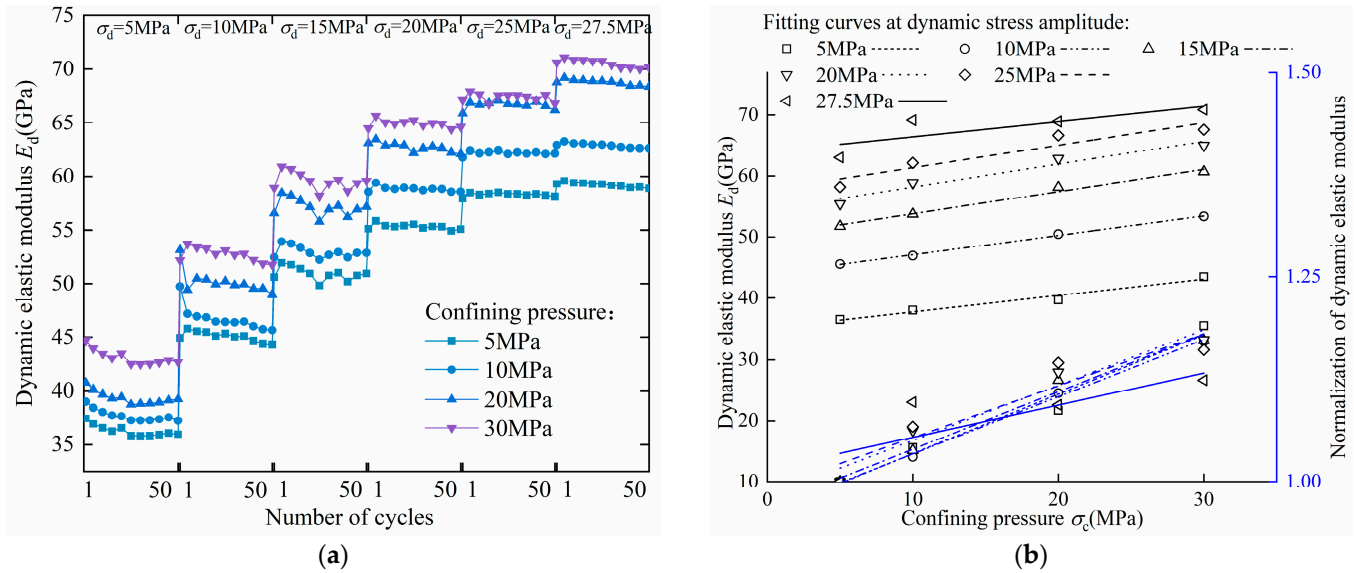


**Figure 9.** Dynamic elastic modulus of specimens with varying confining pressure: (a) the dynamic elastic modulus of the specimens; (b) the average dynamic elastic modulus of the specimens.

To depict more accurately the trend of the dynamic elastic modulus with varying confining pressure, the average dynamic elastic modulus of the specimens with increasing confining pressure at different dynamic stress amplitudes is shown with black curves in Figure 9b, with the data points corresponding to the black y-axis. The average dynamic elastic modulus of the specimens demonstrates an increasing trend with the rise of the confining pressure, with a nearly linear relationship. The inclinations for different stress amplitudes are almost identical. The blue curve, obtained by normalizing the data (normalized with the starting modulus at each line), effectively represents the trend of the average dynamic elastic modulus of the specimens, with the data points corresponding to the blue y-axis. The variation of the fitted curves for dynamic stress amplitude from 5 to 25 MPa shows a consistent pattern. However, the dynamic stress amplitude of 27.5 MPa is close to the maximum dynamic stress amplitude required for the specimen to reach damage, causing a change in the curve’s slope.

The observed increase in the dynamic elastic modulus of the specimens with the rise in the confining pressure is in line with the findings reported by Yang [49] and Li [50]. As the confining pressure increases, the closure of microdefects within the specimen occurs [50,51], resulting in a more compact and damage-resistant state. Consequently, this phenomenon contributes to the enhancement of the dynamic elastic modulus.

Figure 10 illustrates the dynamic damping ratio of the specimens under investigation. Figure 10a presents the impact of the confining pressure, dynamic stress amplitude, and number of cycles on the dynamic damping ratio. It reveals that the dynamic damping ratio of the specimens declined with the increasing number of cycles, confining pressure, and dynamic stress amplitude. To better elucidate the relationship between the dynamic damping ratio and confining pressure, the average dynamic damping ratio of the specimen is plotted against increasing confining pressure at various dynamic stress amplitudes (represented by black curves) in Figure 10b, with the data points corresponding to the black y-axis on the left. Notably, we observe a decrease in the dynamic damping ratio of the specimens as the confining pressure rises. This relationship appears to exhibit a linear trend. The blue curve (located at the bottom of Figure 10b), obtained by normalizing the data

(normalized with the starting damping ratio at each line), effectively represents the trend of the average dynamic damping ratio of the specimens, with the data points corresponding to the blue y-axis on the right. Furthermore, it is evident that the rate of decrease in the dynamic damping ratio of the specimens diminishes as the confining pressure increases at higher dynamic stress amplitudes.

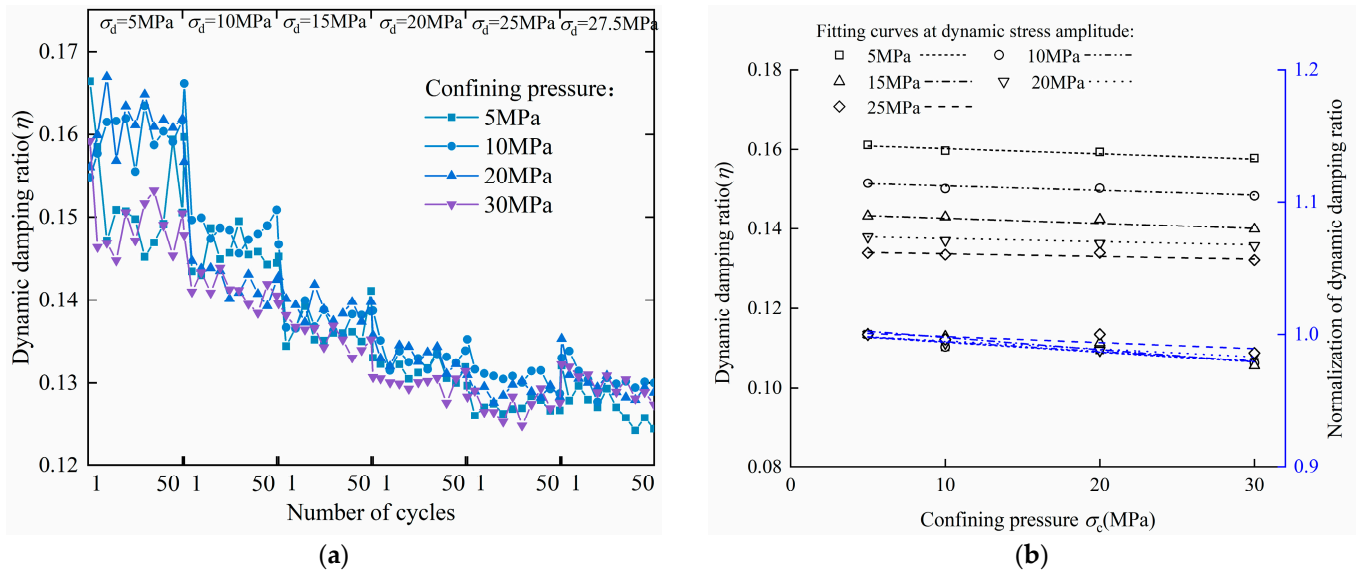


**Figure 10.** Dynamic damping ratio of specimens with varying confining pressure: (a) the dynamic damping ratio of the specimens; (b) the average dynamic damping ratio of the specimens.

With the increase in confining pressure, closure of microdefects within the specimens was observed, leading to a gradual reduction in energy consumption [50,51]. Additionally, the energy dissipation resulting from friction and viscous resistance between the particles and the fluid inside the specimens decreased under cyclic loading conditions [52,53]. The observed decline in the dynamic damping ratio of the specimens can be attributed to the combined effect of these two factors.

#### 4.2.2. Effect of Loading Frequency

Figure 11 presents the variations in the dynamic elastic modulus of the specimens. Figure 11a illustrates the influence of the dynamic elastic modulus of the specimens concerning the frequency, dynamic stress amplitude, and number of cycles. It reveals that the dynamic elastic modulus of the specimens decreased with the increasing number of cycles, while it increased with the increasing frequency and dynamic stress amplitude. At frequencies ranging from 1 to 10 Hz, the dynamic elastic modulus of the specimens exhibits a similar trend at the same dynamic stress amplitude, with relatively small fluctuations across the different number of cycles. However, at the frequency of 20 Hz, the dynamic elastic modulus of the specimens experienced a notable increase, with considerable fluctuations observed for each number of cycles. Specifically, the dynamic elastic modulus of the specimen increased by approximately 7% from 1 Hz to 5 Hz, by about 28% from 1 Hz to 10 Hz, and significantly rose by around 80% from 1 Hz to 20 Hz. To portray more effectively the trend of the dynamic elastic modulus with varying frequencies, we depict the variation of the average dynamic elastic modulus with increasing frequency at different dynamic stress amplitudes using black curves in Figure 11b, with the data points corresponding to the black y-axis on the left. As the frequency increases, the dynamic elastic modulus of the specimen demonstrates a rising trend, and we conjecture that the relationship between them follows a quadratic polynomial pattern. The blue curve, acquired through data normalization, adequately represents the trend of the average dynamic elastic modulus of the specimens, with the data points corresponding to the blue y-axis on the right. Furthermore,

it can be observed that the rate of growth of the dynamic damping ratio of the specimen decelerates as the frequency increases, especially at high dynamic stress amplitude.

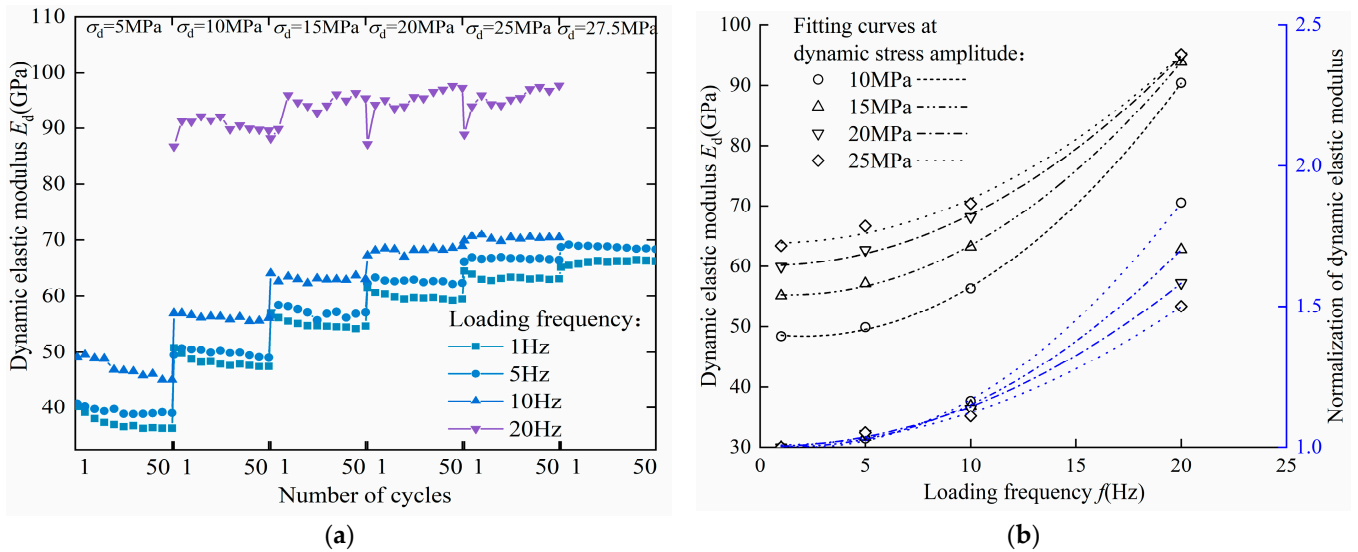


**Figure 11.** Dynamic elastic modulus of specimens with frequencies: (a) the dynamic elastic modulus of the specimens; (b) the average dynamic elastic modulus of the specimens.

During the frequency loading, the particles generated inside the specimens infiltrated into the microscopic cracks, thereby inducing the closure of these cracks [54]. Additionally, the viscosity of the fluid between the mineral particles inside the specimens exhibited an increase with the rise in loading frequency. Consequently, these combined effects enhanced the specimens’ resistance to deformation, resulting in an increase in the dynamic elastic modulus.

The dynamic damping ratio of the specimens is presented in Figure 12. Figure 12a illustrates the impact of frequency, dynamic stress amplitude, and number of cycles on the dynamic damping ratio of the specimens. The dynamic damping ratio decreases with an increase in the number of cycles, rises with an increase in frequency, and declines with an increase in dynamic stress amplitude. Notably, at frequencies of 1–10 Hz, the dynamic damping ratio undergoes minor variations across the number of cycles. However, at a frequency of 20 Hz, the dynamic damping ratio exhibits a substantial increase, and its variation range becomes more pronounced as the number of cycles progress. To elucidate the dynamic damping ratio trend with different frequencies, the average dynamic damping ratio of the specimens with increasing frequency at various dynamic stress amplitudes is depicted using black curves in Figure 12b. A positive correlation between the dynamic damping ratio and frequency is observed. We hypothesize a power function relationship between them. The nearly overlapping black curves suggest a consistent growth rate of the dynamic damping ratio among the specimens. The experimental findings align with those of Zhu et al. [55], where it was noted that the accumulation of fine damage within the rock increased with elevated loading frequency, indicating enhanced energy dissipation inside the rock. As a result, the dynamic damping ratio of the specimens experienced an increase.

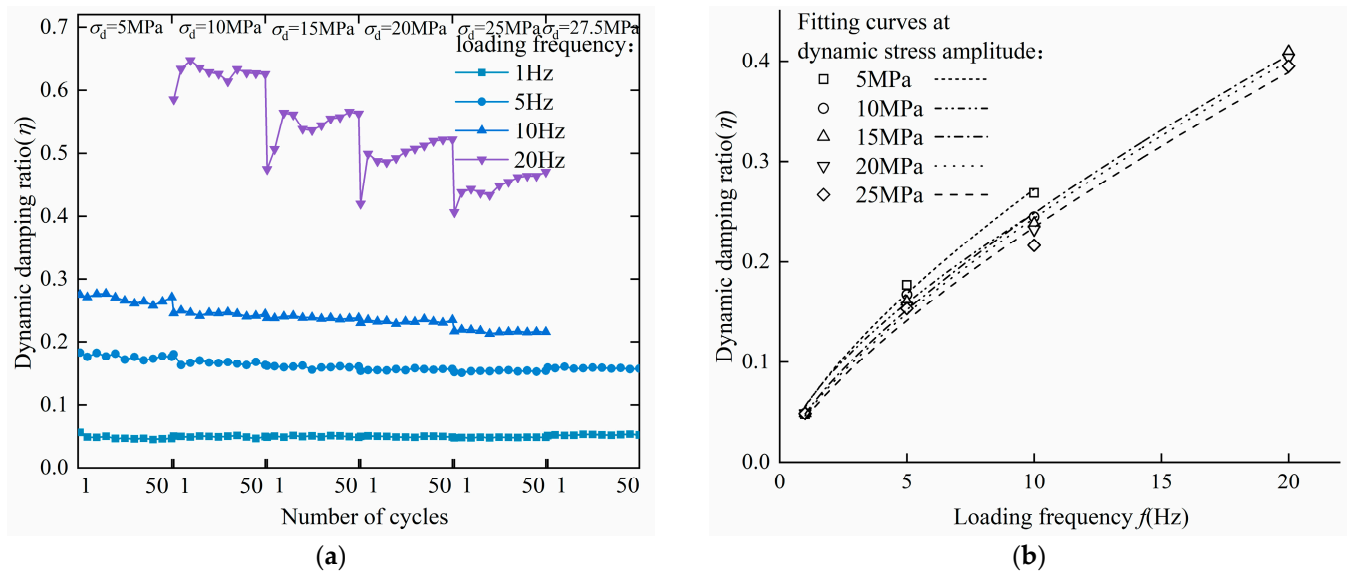


**Figure 12.** Dynamic damping ratio of specimens with frequencies: (a) the dynamic damping ratio of the specimens; (b) the average dynamic damping ratio of the specimens.

#### 4.2.3. Effect of Dynamic Stress Amplitude

Figure 13a,b illustrate the dynamic elastic modulus variations of the specimens under different confining pressures and frequencies. Figure 13a displays the variation of the dynamic elastic modulus with increasing dynamic stress amplitude at various confining pressures, represented by the black curves, with the data points corresponding to the black y-axis. Similarly, Figure 13b depicts the dynamic elastic modulus with increasing dynamic stress amplitude at different frequencies, using the black curves. The blue curves, obtained by normalizing the data separately, reveal the trends in the dynamic elastic modulus of the specimens, with the data points corresponding to the blue y-axis. In Figure 13a, the dynamic elastic modulus of the specimens increases as the dynamic stress amplitude rises. Nevertheless, under high confining pressure, the growth rate of the dynamic elastic modulus slows down with increasing dynamic stress amplitude. We postulate that the relationship between the dynamic elastic modulus and dynamic stress amplitude follows a power function. In Figure 13b, it can be observed that the dynamic elastic modulus of the specimens increases with the increment of dynamic stress amplitude. Notably, at high frequencies, the growth rate of the dynamic elastic modulus diminishes with increasing dynamic stress amplitude. We hypothesize a power-function correlation between the dynamic elastic modulus and dynamic stress amplitude. Furthermore, the increase in the dynamic elastic modulus of the specimen is more pronounced at a frequency of 10 Hz. This pattern is consistent in both Figure 13a,b. During the loading of dynamic stress amplitude, the particles inside the specimen undergo compression, leading to a tighter inter-particle contact. Consequently, the rock stiffness increases, resulting in an elevated dynamic elastic modulus of the specimen.

Figure 14a,b present the dynamic damping ratio variations of the specimens. In Figure 14a, the dynamic damping ratio of the specimens decreases with increasing dynamic stress amplitude, as indicated by the black curves, with the data points corresponding to the black y-axis. We postulate that the relationship between them follows a power function. Moreover, the blue curves, obtained by normalizing the data separately, reveal the trends in the dynamic elastic modulus of the specimens, with the data points corresponding to the blue y-axis. We can see that with the increment of confining pressure, the dynamic damping ratio of the specimens exhibits a slower rate of decrease with increasing dynamic stress amplitude. Figure 14b reveals that the dynamic damping ratio of the specimens decreases with increasing dynamic stress amplitude, displaying a potential power-function relationship between them. Furthermore, the dynamic damping

ratio of the specimens declines at a faster rate with the increase of frequency and dynamic stress amplitude. This phenomenon is attributed to the tightening of contact between mineral particles inside the specimen due to the increase in dynamic stress amplitude. Consequently, the energy consumption resulting from frictional and viscous resistance inside the specimen diminishes as a proportion of the total energy consumption at high dynamic stress amplitudes [52,53], leading to a decrease in the dynamic damping ratio.

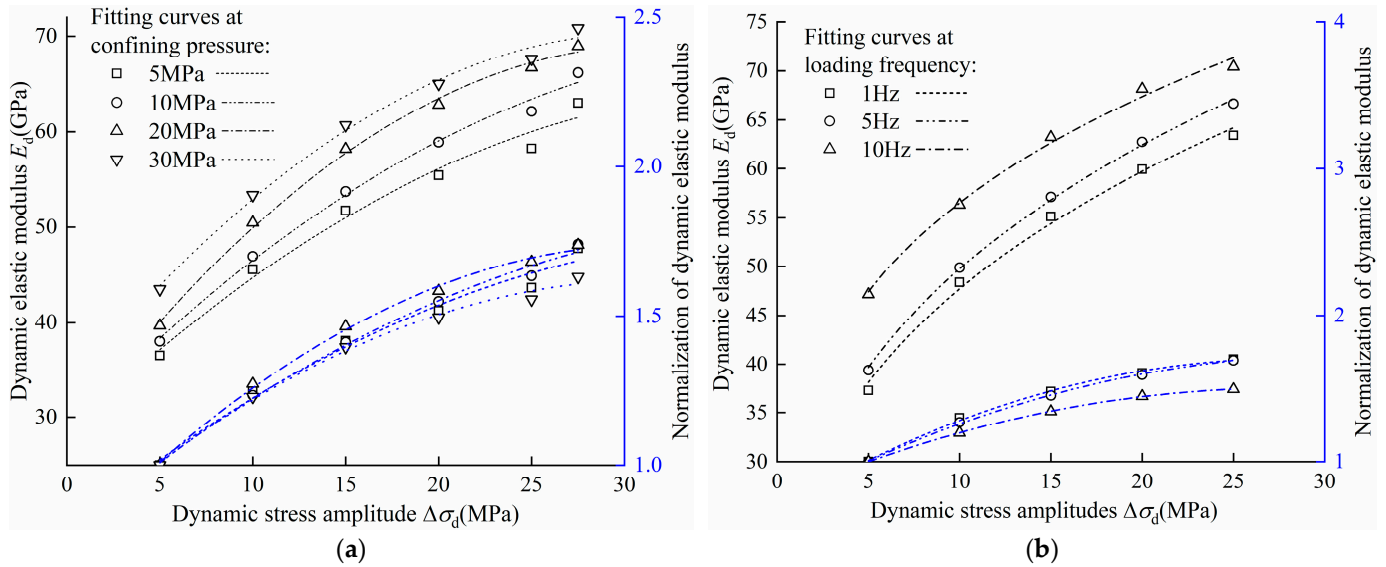


Figure 13. Dynamic elastic modulus of specimens: with dynamic stress amplitude (a) confining pressure; (b) loading frequency.

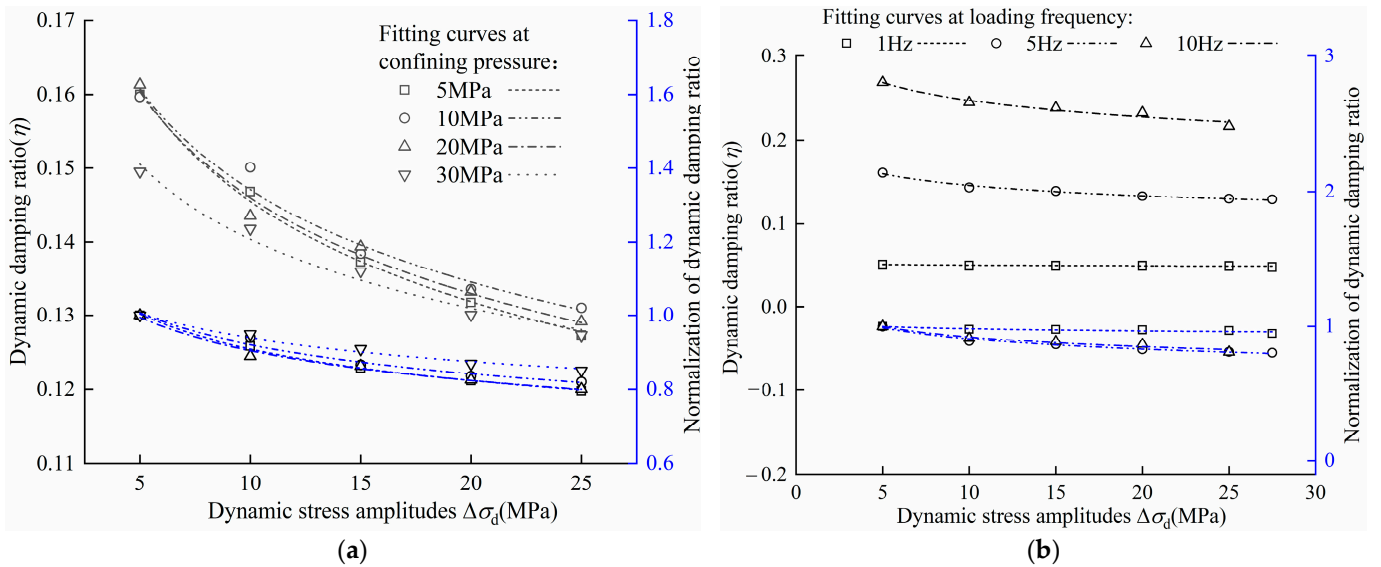
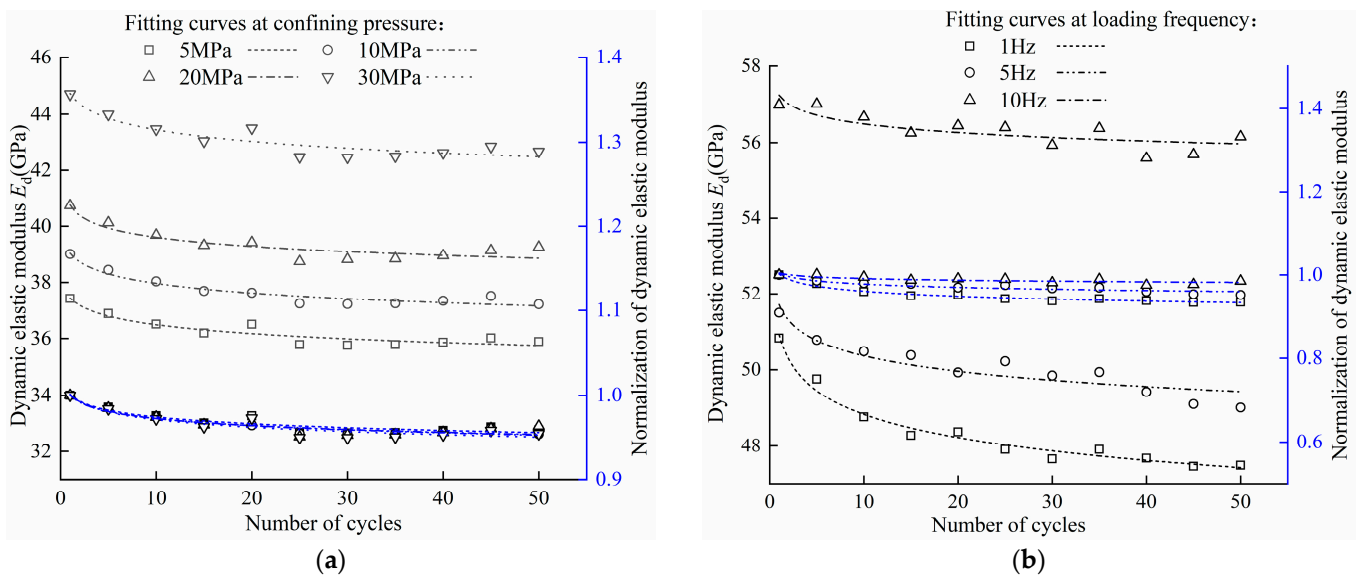


Figure 14. Dynamic damping ratio of specimens: with dynamic stress amplitude (a) confining pressure; (b) loading frequency.

#### 4.2.4. Effect of Number of Cycles

Figure 15 illustrates the dynamic elastic modulus variations of the specimens. In Figure 15a, the black curves represent the variation of the dynamic elastic modulus of the specimens with an increasing number of cycles at different confining pressures, with the data points corresponding to the black y-axis. It is evident that the dynamic elastic modulus of the specimens decreases with an increase in the number of cycles. With the

data points corresponding to the blue y-axis, the nearly overlapping blue curves indicate a similar reduction in the dynamic elastic modulus caused by damage at different confining pressures. We propose a power function relationship based on the black curve to describe this behavior. In Figure 15b, the black curves portray the dynamic elastic modulus of the specimens at different frequencies with increasing numbers of cycles. The dynamic elastic modulus of the specimens decreases as the number of cycles increases. The rate of decrease in the dynamic elastic modulus slows down during loading at high frequencies. We conjecture a power-function relationship between the dynamic elastic modulus of the specimen and the number of cycles. Notably, during the initial stages of loading, the dynamic elastic modulus of the specimens decreases rapidly and gradually stabilizes as the loading progresses. This observation aligns with the findings reported by Ma et al. [56], who indicated that the specimen undergoes progressive irreversible deformation as the loading continues.



**Figure 15.** Dynamic elastic modulus of specimens: with number of cycles (a) confining pressure; (b) loading frequency.

Figure 16a,b depict the dynamic damping ratio variations of the specimens. In Figure 16a, we observe the dynamic damping ratio of the specimen according to the number of cycles at different confining pressures, the black curve corresponds to the black y-axis. The dynamic damping ratio demonstrates a decreasing trend with loading. Figure 16b displays the dynamic damping ratio variation of the specimen according to the number of cycles at different frequencies. The blue curve corresponds to the blue y-axis. Here, the dynamic damping ratio of the specimen exhibits a declining trend as the number of cycles increases. Notably, the dynamic damping ratio varies significantly over a wide range at different frequencies during the loading process. The initial loading stage is characterized by the adjustment of mineral particles inside the specimen, resulting in substantial energy consumption [57]. However, as the particle alignment stabilizes, the energy consumed by the specimen gradually diminishes. Concurrently, the cumulative damage to the specimen increases throughout the loading process [58].



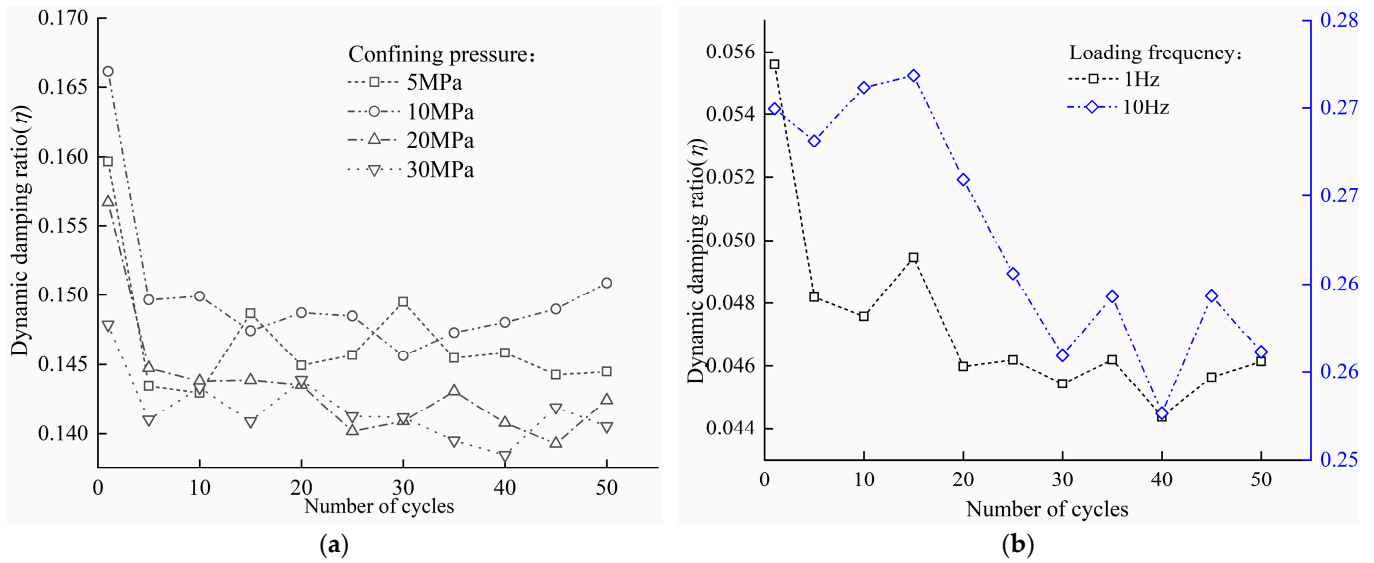


**Figure 16.** Dynamic damping ratio of specimens: with number of cycles (a) confining pressure; (b) loading frequency.

## 5. Dynamic Response Model

### 5.1. Model Establishment

The Duncan–Chang model [59], known for its capability to accurately describe the stress–strain behavior of rock, has been extensively utilized by researchers [60,61] to analyze the variations in rock stress–strain. Although originally proposed for static loading conditions, we applied the Duncan–Chang model in this study, considering the frequency range of 1–20 Hz used in our tests, which can be considered as quasi-static conditions. As such, we have opted for the Duncan–Chang model to effectively characterize the relationship between dynamic stress and dynamic strain amplitudes of the specimens.

The relationship between the dynamic stress and dynamic strain amplitude of the specimens is as follows:

$$\sigma_d = \frac{\Delta \varepsilon_d}{a + b \Delta \varepsilon_d} \quad (3)$$

where  $\sigma_d$  is dynamic stress level,  $\Delta \varepsilon_d$  is dynamic strain amplitude, and  $a$  and  $b$  are test parameters.

Figure 17 depicts the relationship between the dynamic stress and dynamic strain amplitude of the specimens at various loading frequencies. A notable observation is the excellent fit of the curve, implying that the model accurately reflects the relationship between the dynamic stress and dynamic strain amplitude of the specimens.

To obtain the significance of the model parameters  $a$  and  $b$ , we transform Equation (3) into the following relationship:

$$\frac{\Delta \varepsilon_d}{\sigma_d} = a + b \Delta \varepsilon_d \quad (4)$$

where  $\sigma_d$  is dynamic stress level,  $\Delta \varepsilon_d$  is dynamic strain amplitude, and  $a$  and  $b$  are test parameters.

In Figure 18, the relationship between the ratio of dynamic strain amplitude to dynamic stress and dynamic strain amplitude is displayed. However, it can be observed that Equation (4) inadequately captures the variations of the material property parameters of the specimens at lower frequencies. Consequently, we postulated that the relationship between the ratio of dynamic strain amplitude to dynamic stress and dynamic strain

amplitude may better conform to a quadratic polynomial curve. To address this, we enhanced the Duncan–Chang model with the following modified formula:

$$\sigma_d = \frac{\Delta\epsilon_d}{a + b\Delta\epsilon_d + c\Delta\epsilon_d^2} \tag{5}$$

$$\frac{\Delta\epsilon_d}{\sigma_d} = a + b\Delta\epsilon_d + c\Delta\epsilon_d^2 \tag{6}$$

where  $\sigma_d$  is dynamic stress level,  $\Delta\epsilon_d$  is dynamic strain amplitude, and  $a$ ,  $b$ , and  $c$  are test parameters.

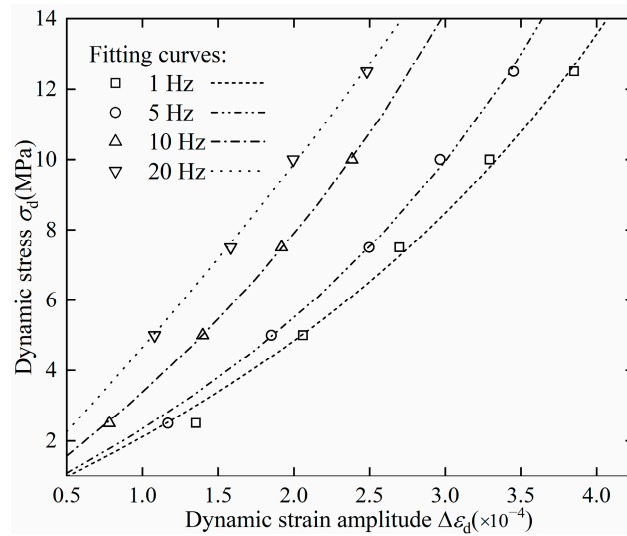


Figure 17. Specimens’ fitting curves for Duncan-Chang model.

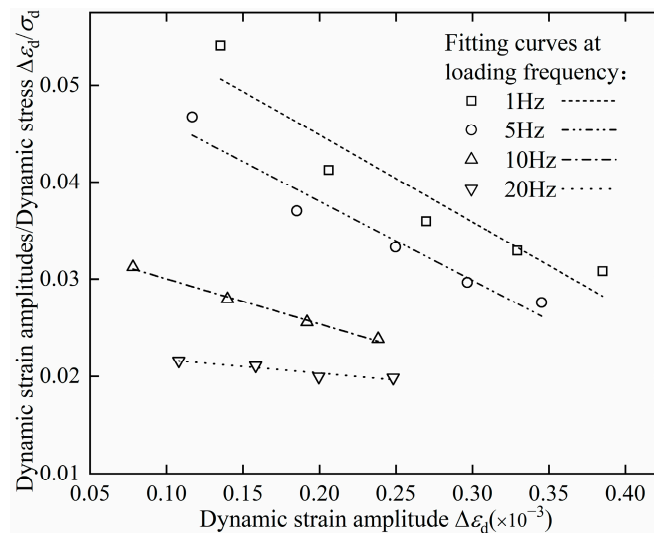


Figure 18. Specimens’  $\Delta\epsilon_d / \sigma_d - \Delta\epsilon_d$  fitting curves for Duncan-Chang model.

### 5.2. Influence of Confining Pressure

In Figure 19, the results of fitting Equation (5) between dynamic strain and dynamic stress are presented. The outcomes reveal that with an increase in the dynamic stress level, the dynamic strain in the specimen also increases. Furthermore, at a consistent dynamic stress level, the dynamic strain in the specimen demonstrates an increment upon reducing the confining pressure. Notably, the improved Duncan–Chang model exhibits a favorable fit to the experimental data.

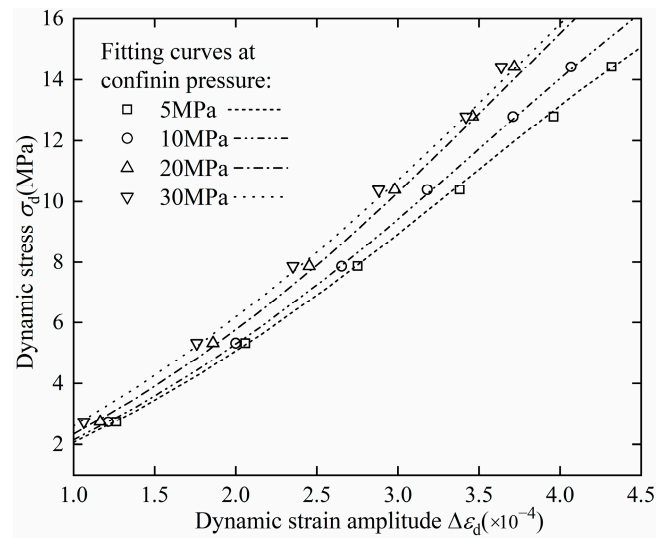


Figure 19. Specimens’ fitting curves with confining pressure.

In Figure 20, the results obtained from fitting Equation (6) between the ratio of dynamic strain amplitude to dynamic stress and dynamic strain amplitude are presented. The findings illustrate a gradual decrease in the ratio of dynamic strain amplitude to dynamic stress as the dynamic stress amplitude increases.

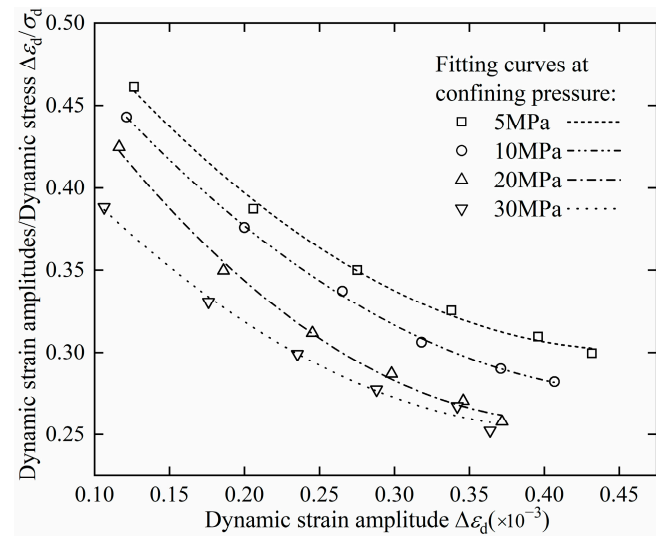


Figure 20. Specimens’  $\Delta\epsilon_d / \sigma_d - \Delta\epsilon_d$  fitting curves with confining pressure.

Table 3 presents the results of fitting Equation (6), with all formulas achieving a correlation coefficient of 0.99. This outcome validates our hypothesis that the relationship between the ratio of dynamic strain amplitude to dynamic stress and dynamic strain amplitude follows a quadratic polynomial pattern. Notably, there is a more pronounced correlation between the ratio of dynamic strain amplitude to dynamic stress and dynamic strain amplitude.

**Table 3.** Equation (6) fitting curve with confining pressure.

Name	Confining Pressure $\sigma_c$ (MPa)	Fitting Formula	Fitting ( $R^2$ )
Granite specimens	5	$y = 0.06 - 0.13x + 0.142x^2$	0.99
	10	$y = 0.058 - 0.127x + 0.133x^2$	0.99
	20	$y = 0.053 - 0.114x + 0.115x^2$	0.99
	30	$y = 0.046 - 0.084x + 0.081x^2$	0.99

Table 4 displays the experimental parameters  $a$ ,  $b$ , and  $c$  concerning the variations in confining pressure. The analysis reveals that the test parameter  $a$  exhibits a linear relationship with confining pressure, while the parameters  $b$  and  $c$  follow a quadratic polynomial trend with respect to changes in confining pressure.

**Table 4.** The change curves of parameters  $a$ ,  $b$ , and  $c$  with confining pressure.

Name	Parameter and Confining Pressure Relationship Formula
Granite specimens	$a = 0.0633 - 0.00056\sigma_c$ $b = -0.128 - 7.76 \times 10^{-4}\sigma_c + 7.4 \times 10^{-5}\sigma_c^2$ $c = 0.144 - 3.89 \times 10^{-4}\sigma_c - 5.7 \times 10^{-5}\sigma_c^2$

### 5.3. Influence of Loading Frequency

Figure 21 illustrates the outcomes of fitting Equation (5) to describe the relationship between dynamic strain and dynamic stress. The results indicate that with an increase in the level of dynamic stress, the dynamic strain of the specimen also rises. Moreover, at the same dynamic stress level, the dynamic strain of the specimen increases with a decrease in the loading frequency.

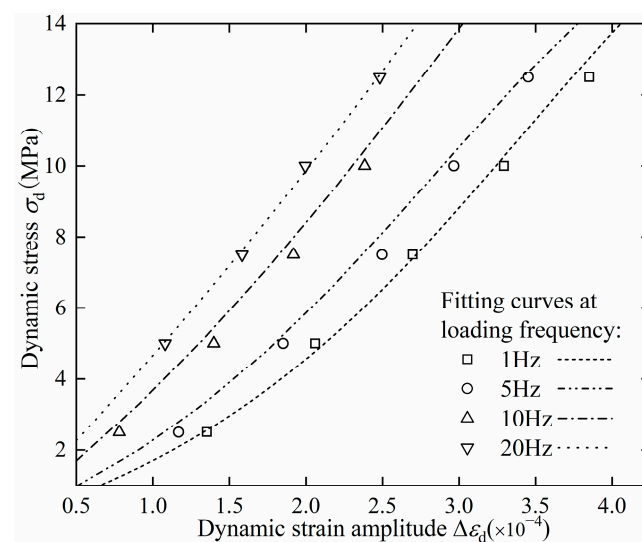


**Figure 21.** Specimens’ fitting curves with loading frequencies.

Figure 22 presents the outcomes of fitting Equation (6) to illustrate the relationship between the ratio of dynamic strain amplitude to dynamic stress and dynamic strain amplitude. The results demonstrate a gradual decrease in the ratio of dynamic strain amplitude to dynamic stress as the dynamic stress amplitude increases.

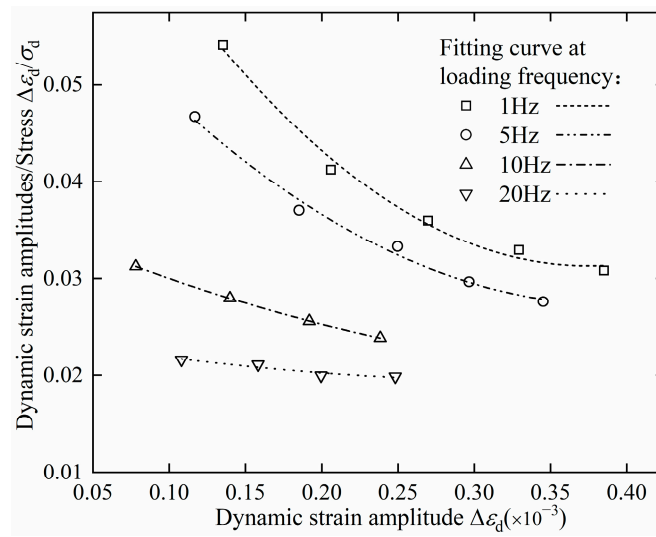


Figure 22. Specimens’  $\Delta\epsilon_d/\sigma_d-\Delta\epsilon_d$  fitting curves with loading frequencies.

Table 5 displays the outcomes of fitting Equation (6) to investigate the relationship between the ratio of dynamic strain amplitude to dynamic stress and dynamic strain amplitude at different frequencies. The correlation coefficients of the formulas for frequencies ranging from 1 to 10 Hz all reach 0.98, supporting our hypothesis that the relationship follows a quadratic polynomial pattern.

Table 5. Equation (6) fitting curve with loading frequencies.

Name	Loading Frequency $f$ (Hz)	Fitting Formula	Fitting ( $R^2$ )
Granite specimens	1	$y = 0.0784 - 0.222x + 0.247x^2$	0.98
	5	$y = 0.0584 - 0.163x + 0.211x^2$	0.98
	10	$y = 0.0319 - 0.053x + 0.062x^2$	0.99
	20	$y = 0.023 - 0.013x + 0.004x^2$	0.75

However, at a frequency of 20 Hz, the correlation coefficient of the fitted formula decreases to 0.75. We attribute this observation to the higher frequency exerting a more significant impact on the specimen compared with the confining pressure, which is consistent with the findings and conclusions presented in Sections 3 and 4. As the next step in our research, we aim to deduce the primary stress field by integrating information from the wave velocity measurements within the tunnel envelope and the characteristics of the internal stress field. This primary stress field will then be employed to modify the formula for material performance parameters, enabling us to derive the initial stress conditions of the specimen.

Table 6 presents the experimental parameters  $a$ ,  $b$ , and  $c$  concerning their variation with loading frequency. The analysis reveals a clear power-function relationship between these parameters ( $a$ ,  $b$ , and  $c$ ) and the loading frequency.

Table 6. The change curves of parameters  $a$ ,  $b$ , and  $c$  with loading frequencies.

Name	Parameter and Loading Frequency Relationship Formula
Granite specimens	$a = 0.0154 + 0.073 \times 0.88^f$
	$b = 0.03 - 0.29 \times 0.90^f$
	$c = -0.102 + 0.39 \times 0.93^f$

## 6. Conclusions

To construct a back-analysis model for a granite sample, we conducted a series of triaxial tests, controlling the confining pressure, loading amplitude, loading frequency, and number of cycles. The dynamic properties of the provided granite sample were meticulously studied, and a dynamic response model was developed using the test data. The following conclusions can be drawn:

1. The dynamic response of granite was examined under various factors, including loading frequency (1–20 Hz), confining pressure (5–30 MPa), dynamic stress amplitude (5–27.5 MPa), and the number of cycles (0–50 times).
2. The dynamic elastic modulus of granite increased by approximately 6%, 13%, and 20% as the dynamic stress amplitude went from 5 MPa to 10 MPa, 20 MPa, and 30 MPa, respectively. This behavior can be attributed to the closure of microdefects and reduced energy consumption. On the contrary, the dynamic damping ratio exhibited a decline due to diminished energy consumption resulting from friction and viscous resistance.
3. Granite's dynamic elastic modulus and dynamic damping ratio displayed an upward trend with loading frequency. The dynamic elastic modulus increased by approximately 7% (from 1 Hz to 5 Hz), 28% (from 1 Hz to 10 Hz), and 80% (from 1 Hz to 20 Hz). Enhanced dynamic stress amplitude led to an increased dynamic elastic modulus and a decreased dynamic damping ratio. These outcomes are associated with microcrack closure, increased intergranular viscosity, and heightened energy consumption.
4. Increasing dynamic stress amplitude resulted in a higher dynamic elastic modulus and a lower dynamic damping ratio. This is attributed to particle compression, leading to tighter contacts and decreased energy consumption from friction and viscous resistance.
5. The dynamic elastic modulus and dynamic damping ratio of granite decreased before stabilizing with an increase in the number of cycles. The initial loading stage induced significant deformation and energy consumption, followed by gradual stabilization as equilibrium was reached.
6. The modified Duncan–Chang model established a dynamic stress–strain relationship for granite and demonstrated good alignment with experimental data. It is noteworthy that high frequency had a more significant impact on material behavior compared with confining pressure. These experimental data and the constructed model will be further integrated into Part II of our research, enabling a comprehensive investigation and a deeper understanding of the proposed study.

**Author Contributions:** Conceptualization, X.D. and M.Z.; Data curation, J.Z. and Y.D.; Funding acquisition, X.D. and M.Z.; Methodology, X.D. and M.Z.; Resources, X.D. and M.Z.; Supervision, X.D.; Writing—original draft, J.Z.; Writing—review & editing, X.D. and J.Z. All authors have read and agreed to the published version of the manuscript.

**Funding:** This research was financially supported by the National Natural Science Foundation of China (Grant No. 41827807, 42276213) and Guangdong Provincial Key Laboratory of Modern Civil Engineering Technology (2021B1212040003). All the sources of support are gratefully acknowledged.

**Institutional Review Board Statement:** Not applicable.

**Informed Consent Statement:** Not applicable.

**Data Availability Statement:** The data presented in this study are available on request from the corresponding author. The data are not publicly available due to the back analysis experiment has not yet been completed.

**Conflicts of Interest:** The authors declare no conflict of interest.

## References

1. Mizuno, A. Report on the collapse accident of the ceiling boards for transverse ventilation at the Sasago Tunnel. In Proceedings of the 17th International Symposium on Aerodynamics, Ventilation and Fire in Tunnels 2017, ISAVFT 2017, Lyon, France, 13–15 September 2017; pp. 621–630.
2. Crampin, S.; Peacock, S. A review of the current understanding of seismic shear-wave splitting in the Earth's crust and common fallacies in interpretation. *Wave Motion* **2008**, *45*, 675–722. [[CrossRef](#)]
3. Bai, Q.; Konietzky, H. An innovative method to simulate stress-induced velocity changes in anisotropic rocks. *Geotech. Lett.* **2021**, *11*, 299–305. [[CrossRef](#)]
4. Tian, J.; Wang, E. Ultrasonic method for measuring in-situ stress based on acoustoelasticity theory. *Yanshilixue Yu Gongcheng Xuebao/Chin. J. Rock Mech. Eng.* **2006**, *25*, 3719–3724.
5. Kang, F.; Jia, T.; Li, Y.; Deng, J.; Tang, C.a.; Huang, X. Experimental study on the physical and mechanical variations of hot granite under different cooling treatments. *Renew. Energy* **2021**, *179*, 1316–1328. [[CrossRef](#)]
6. Yang, S.Q.; Li, Y.; Ma, G.W.; Sun, B.W.; Yang, J.; Xu, J.; Dai, Y.H. Experiment and numerical simulation study of dynamic mechanical behavior of granite specimen after high temperature treatment. *Comput. Geotech.* **2023**, *154*, 105111. [[CrossRef](#)]
7. Liu, X.; Zheng, Y.; Hao, Q.; Zhao, R.; Xue, Y.; Zhang, Z. Dynamic failure features and brittleness evaluation of coal under different confining pressure. *Geomech. Eng.* **2022**, *30*, 401–411. [[CrossRef](#)]
8. Chongyang, W.; Sijiang, W.; Yisha, P.; Sheng, Z. Experimental Study on Fatigue Life of Gypsum-Like Rock Under Uniaxial Compression with Different Loading Frequencies. *Pure Appl. Geophys.* **2022**, *179*, 1225–1239. [[CrossRef](#)]
9. Zheng, Q.; Liu, E.; Sun, P.; Liu, M.; Yu, D. Dynamic and damage properties of artificial jointed rock samples subjected to cyclic triaxial loading at various frequencies. *Int. J. Rock Mech. Min. Sci.* **2020**, *128*, 104243. [[CrossRef](#)]
10. Chen, Z.; Ma, C.; Li, T.; He, C. Experimental investigation of the failure mechanism of deep granite under high seepage water pressure and strong unloading effect. *Acta Geotech.* **2022**, *17*, 5009–5030. [[CrossRef](#)]
11. Deng, L.; Wu, Y.; Ji, Y.; Huang, Z.; Zou, C. Physical and mechanical properties of granite after high-temperature and acidic treatment for the enhanced geothermal system. *Bull. Eng. Geol. Environ.* **2022**, *81*, 407. [[CrossRef](#)]
12. Chen, Y.-L.; Wang, S.-R.; Ni, J.; Azzam, R.; Fernández-steeger, T.M. An experimental study of the mechanical properties of granite after high temperature exposure based on mineral characteristics. *Eng. Geol.* **2017**, *220*, 234–242. [[CrossRef](#)]
13. Liu, L.; Wang, Y.; An, H. Fractal Characteristics and Energy Dissipation of Granite After High-Temperature Treatment Based on SHPB Experiment. *Front. Earth Sci.* **2022**, *10*, 861847. [[CrossRef](#)]
14. Gao, C.; Zhou, Z.; Li, L.; Li, Z.; Zhang, D.; Cheng, S. Strength reduction model for jointed rock masses and peridynamics simulation of uniaxial compression testing. *Geomech. Geophys. Geo-Energy Geo-Resour.* **2021**, *7*, 34. [[CrossRef](#)]
15. As'habi, F.; Lakirouhani, A. Numerical modeling of jointed rock samples under unconfined and confined conditions to study peak strength and failure mode. *Arab. J. Geosci.* **2021**, *14*, 174. [[CrossRef](#)]
16. Ma, Z.; Yan, P.; Cheng, S.; Gong, P.; Qi, F.; Wang, J. Experimental study of the dynamic mechanical responses and failure characteristics of coal under true triaxial confinements. *Int. J. Min. Sci. Technol.* **2023**, *33*, 761–772. [[CrossRef](#)]
17. Yang, B.; He, M.; Zhang, Z.; Zhu, J.; Chen, Y. Experimental investigation and empirical model on damping properties of rock under multistage cyclic loading. *Soil Dyn. Earthq. Eng.* **2022**, *163*, 107557. [[CrossRef](#)]
18. Ma, C.; Zhu, C.; Zhou, J.; Ren, J.; Yu, Q. Dynamic response and failure characteristics of combined rocks under confining pressure. *Sci. Rep.* **2022**, *12*, 12187. [[CrossRef](#)]
19. Yan, Z.Q.; Li, Z.; Tan, Y.Z.; Ma, L.J.; Yu, L.Y.; Li, H.Y. Coupling Effects of Strain Rate and Low Temperature on the Dynamic Mechanical Properties of Frozen Water-Saturated Sandstone. *Water* **2022**, *14*, 3513. [[CrossRef](#)]
20. Suo, Y.; Su, X.; Wang, Z.; He, W.; Fu, X.; Feng, F.; Pan, Z.; Xie, K.; Wang, G. A study of inter-stratum propagation of hydraulic fracture of sandstone-shale interbedded shale oil. *Eng. Fract. Mech.* **2022**, *275*, 108858. [[CrossRef](#)]
21. Su, H.; Jiang, Y.; Yu, L.; Wang, W.; Guo, Q. Dynamic fracture and deformation responses of rock mass specimens containing 3D printing rough joint subjected to impact loading. *Geomech. Geophys. Geo-Energy Geo-Resour.* **2022**, *8*, 186. [[CrossRef](#)]
22. Ni, X.H. Failure characteristic of granite under cyclic loading with different frequencies. *Appl. Mech. Mater.* **2014**, *638–640*, 1967–1970. [[CrossRef](#)]
23. Fu, B.; Zhang, D.; Ye, C. Experimental Study on Mechanical Properties of Sandstone Under Sinusoidal Dynamic Load. *Geotech. Geol. Eng.* **2022**, *40*, 2397–2408. [[CrossRef](#)]
24. Luo, Y.; Gong, H.; Wei, X.; Zheng, S.; Pei, C.; Li, X. Dynamic compressive characteristics and damage constitutive model of coral reef limestone with different cementation degrees. *Constr. Build. Mater.* **2023**, *362*, 129783. [[CrossRef](#)]
25. Mishra, S.; Khetwal, A.; Chakraborty, T.; Basu, D. Effect of loading characteristics and specimen size in split Hopkinson pressure bar test on high-rate behavior of phyllite. *Arch. Civ. Mech. Eng.* **2022**, *22*, 212. [[CrossRef](#)]
26. Han, Z.; Xie, S.; Li, D.; Zhu, Q.; Yan, Z. Dynamic mechanical behavior of rocks containing double elliptical inclusions at various inclination angles. *Theor. Appl. Fract. Mech.* **2022**, *121*, 103544. [[CrossRef](#)]
27. Liu, Y.; Dai, F.; Dong, L.; Xu, N.; Feng, P. Experimental Investigation on the Fatigue Mechanical Properties of Intermittently Jointed Rock Models Under Cyclic Uniaxial Compression with Different Loading Parameters. *Rock Mech. Rock Eng.* **2017**, *51*, 47–68. [[CrossRef](#)]
28. Manogharan, P.; Wood, C.; Marone, C.; Elsworth, D.; Rivière, J.; Shokouhi, P. Experimental Investigation of Elastodynamic Nonlinear Response of Dry Intact, Fractured and Saturated Rock. *Rock Mech. Rock Eng.* **2021**, *55*, 2665–2678. [[CrossRef](#)]

29. He, M.M.; Zhang, Z.Q.; Li, N. Experimental investigation and empirical model to determine the damping and shear stiffness properties of soft rock under multistage cyclic loading. *Soil Dyn. Earthq. Eng.* **2021**, *147*, 106818. [[CrossRef](#)]
30. Mishra, S.; Chakraborty, T.; Matsagar, V.; Loukus, J.; Bekkala, B. High Strain-Rate Characterization of Deccan Trap Rocks Using SHPB Device. *J. Mater. Civ. Eng.* **2018**, *30*, 04018059. [[CrossRef](#)]
31. Guo, H.; Guo, W.; Zhai, Y.; Su, Y. Experimental and modeling investigation on the dynamic response of granite after high-temperature treatment under different pressures. *Constr. Build. Mater.* **2017**, *155*, 427–440. [[CrossRef](#)]
32. Wang, X.; Liu, Z.; Gao, X.; Li, P.; Dong, B. Dynamic characteristics and energy evolution of granite subjected to coupled static–cyclic impact loading. *Geomech. Geophys. Geo-Energy Geo-Resour.* **2023**, *9*, 62. [[CrossRef](#)]
33. Wang, H.; He, M.; Zhu, J.; Guo, S.; Chen, Y.; Li, N. Experimental investigation of linear damping characteristics on granite and red sandstone under dynamic cyclic loading. *Eur. J. Environ. Civ. Eng.* **2022**, *26*, 5259–5278. [[CrossRef](#)]
34. Li, P.; Cai, M.; Gao, Y.; Guo, Q.; Miao, S.; Ren, F.; Wang, Y. Mechanical responses and fracturing behavior of jointed rock masses with a cavity under different dynamic loads. *Int. J. Impact Eng.* **2023**, *178*, 104608. [[CrossRef](#)]
35. Chen, D.; Tang, J.; Yang, X. Effects of Drying&ndash;Wetting Cycle and Fines Content on Hysteresis and Dynamic Properties of Granite Residual Soil under Cyclic Loading. *Appl. Sci.* **2023**, *13*, 6660.
36. Xia, W.; Xue, J.; Zhang, Y.; Jin, J.; Zhao, Z.; Cai, R. Dynamic Characteristics of Thermal Damage Granite Under Cyclic Impact Loading. *Geotech. Geol. Eng.* **2023**, *41*, 2313–2323. [[CrossRef](#)]
37. Sun, B.; Yang, P.; Liu, S.; Zeng, S. Impact dynamic characteristics and constitutive model of granite damaged by cyclic loading. *J. Mater. Res. Technol.* **2023**, *24*, 333–345. [[CrossRef](#)]
38. Zhang, H.; Huang, L.; Li, X.; Hu, X.; Wu, Y. Study on the Evolution of Physical Parameters and Dynamic Compression Mechanical Properties of Granite after Different Heating and Cooling Cycles. *Materials* **2023**, *16*, 2300. [[CrossRef](#)]
39. Xi, Y.; Wang, H.; Zha, C.; Li, J.; Guo, B. Experimental study of the influence of temperature and cooling method on dynamic mechanical properties and damage of granite. *Energy Sci. Eng.* **2022**, *10*, 3779–3797. [[CrossRef](#)]
40. Li, G.; Liu, S.; Lu, R.; Ma, F.; Guo, J. Experimental Study on Mechanical Properties and Failure Laws of Granite with Artificial Flaws under Coupled Static and Dynamic Loads. *Materials* **2022**, *15*, 6105. [[CrossRef](#)]
41. Tian, N.; Wang, Z.; Xiong, F.; Liu, Z. Influence of axial pressure on dynamic mechanical properties of granite under cyclic impact loading. *Harbin Gongye Daxue Xuebao/J. Harbin Inst. Technol.* **2021**, *53*, 156–164. [[CrossRef](#)]
42. Xiao, P.; Li, D.-y.; Zhao, G.-y.; Zhu, Q.-q.; Liu, H.-x.; Zhang, C.-s. Mechanical properties and failure behavior of rock with different flaw inclinations under coupled static and dynamic loads. *J. Cent. South Univ.* **2020**, *27*, 2945–2958. [[CrossRef](#)]
43. Li, D.; Hu, C.; Zhu, Q. Experimental study on mechanical properties and failure laws of granite with an artificial flaw under coupled static and dynamic loads. *Yanshilixue Yu Gongcheng Xuebao/Chin. J. Rock Mech. Eng.* **2020**, *39*, 6105. [[CrossRef](#)]
44. Chen, Y.; Zuo, J.; Guo, B.; Guo, W. Effect of cyclic loading on mechanical and ultrasonic properties of granite from Maluanshan Tunnel. *Bull. Eng. Geol. Environ.* **2020**, *79*, 299–311. [[CrossRef](#)]
45. Liang, S.; Ling, T.; Liu, D.; Li, S. On Dynamic Constitutive Model of Granite Under Impact Loading: Effect of Damage on Dynamic Strength. *IOP Conf. Ser. Earth Environ. Sci.* **2019**, *283*, 012019. [[CrossRef](#)]
46. Zhao, Z.; Wu, B.; Zhang, Z.; Yu, W. Impact strength characteristics of granite under combined dynamic and static loading conditions. *Arab. J. Geosci.* **2021**, *14*, 105. [[CrossRef](#)]
47. Bie, P.F.; Liu, H.X. Influence of stress amplitude on the dynamic characteristics of phyllite samples under triaxial multi-stage cyclic loading. *IOP Conf. Ser. Earth Environ. Sci.* **2020**, *570*, 032043. [[CrossRef](#)]
48. BJ, B.; FD, S. Frequency dependence of elasticity of rock—Test of seismic velocity. *Nature* **1977**, *268*, 220–222.
49. Yang, S.-Q.; Tang, J.-Z.; Wang, S.-S.; Yang, D.-S.; Zheng, W.-T. An Experimental and Modeling Investigation on Creep Mechanical Behavior of Granite Under Triaxial Cyclic Loading and Unloading. *Rock Mech. Rock Eng.* **2022**, *55*, 5577–5597. [[CrossRef](#)]
50. Qian, L.; Yao, T.; Mo, Z.; Gao, Y.; Zhang, J.; Li, Y.; Zhang, R.; Li, Z. Experimental study on crack evolution behavior and constitutive model of granite based on the deviatoric stress to peak strength ratio. *Bull. Eng. Geol. Environ.* **2022**, *81*, 278. [[CrossRef](#)]
51. Meng, Q.B.; Liu, J.F.; Huang, B.X.; Pu, H.; Wu, J.Y.; Zhang, Z.Z. Effects of Confining Pressure and Temperature on the Energy Evolution of Rocks Under Triaxial Cyclic Loading and Unloading Conditions. *Rock Mech. Rock Eng.* **2022**, *55*, 773–798. [[CrossRef](#)]
52. Tutuncu, A.N.; Podio, A.L.; Sharma, M.M. Nonlinear viscoelastic behavior of sedimentary rocks, Part II: Hysteresis effects and influence of type of fluid on elastic moduli. *Geophysics* **1998**, *63*, 195–203. [[CrossRef](#)]
53. David, E.C.; Brantut, N.; Schubnel, A.; Zimmerman, R.W. Sliding crack model for nonlinearity and hysteresis in the uniaxial stress–strain curve of rock. *Int. J. Rock Mech. Min. Sci.* **2012**, *52*, 9–17. [[CrossRef](#)]
54. Zhu, Z.D.; Ni, X.; Hu, Z.; Huang, Q.; Li, X. Mesoscopic damage quantification research of the deformation and failure of granite under circulatory load with different frequencies. *Eur. J. Environ. Civ. Eng.* **2013**, *17*, s321–s333. [[CrossRef](#)]
55. Zhu, Z.D.; Sun, L.Z.; Wang, M.Y. Damping ratio experiment and mesomechanical analysis of deformation failure mechanism on rock under different frequency cyclic loadings. *Yantu Lixue/Rock Soil Mech.* **2010**, *31*, 8–12.
56. Ma, L.J.; Liu, X.Y.; Wang, M.Y.; Xu, H.F.; Hua, R.P.; Fan, P.X.; Jiang, S.R.; Wang, G.A.; Yi, Q.K. Experimental investigation of the mechanical properties of rock salt under triaxial cyclic loading. *Int. J. Rock Mech. Min. Sci.* **2013**, *62*, 34–41. [[CrossRef](#)]
57. Liu, J.; Qiao, L.; Li, P. Experimental studies and constitutive model of elastoplastic mechanical behaviors of sandstone with hydro-physicochemical influencing effects. *Yanshilixue Yu Gongcheng Xuebao/Chin. J. Rock Mech. Eng.* **2009**, *28*, 20–29. [[CrossRef](#)]
58. Fan, J.; Jiang, D.; Liu, W.; Wu, F.; Chen, J.; Daemen, J. Discontinuous fatigue of salt rock with low-stress intervals. *Int. J. Rock Mech. Min. Sci.* **2019**, *115*, 77–86. [[CrossRef](#)]



59. Duncan, J.M.; Chang, C.Y.; Division, F. Nonlinear Analysis of Stress and Strain in Soils. *J. Soil Mech. Found. Div.* **1970**, *96*, 1629–1653. [[CrossRef](#)]
60. Jia, P.; Khoshghalb, A.; Chen, C.; Zhao, W.; Dong, M.; Alipour Esgandani, G. Modified Duncan-Chang Constitutive Model for Modeling Supported Excavations in Granular Soils. *Int. J. Geomech.* **2020**, *20*, 04020211. [[CrossRef](#)]
61. Yang, S.Q.; Yang, J.; Xu, P. Analysis on pre-peak deformation and energy dissipation characteristics of sandstone under triaxial cyclic loading. *Geomech. Geophys. Geo-Energy Geo-Resour.* **2020**, *6*, 24. [[CrossRef](#)]

**Disclaimer/Publisher’s Note:** The statements, opinions and data contained in all publications are solely those of the individual author(s) and contributor(s) and not of MDPI and/or the editor(s). MDPI and/or the editor(s) disclaim responsibility for any injury to people or property resulting from any ideas, methods, instructions or products referred to in the content.